Spring 1-1-2016

The Effects of Time Step on Reynolds Averaged Navier-Stokes Simulations of High-Lift Flows

Riccardo Balin

University of Colorado Boulder, riccardo.balin@colorado.edu

www.manaraa.com

The Effects of Time Step on Reynolds Averaged Navier-Stokes

Simulations of High-Lift Flows

by

Riccardo Balin

A thesis submitted to the

Faculty of the of the Graduate School of the

University of Colorado in partial fulfillment

Of the requirement for the degree of

Master of Science

Department of Aerospace Engineering Sciences

2016

This thesis entitled:
The Effects of Time Step on Reynolds Averaged Navier-Stokes Simulations of High-Lift Flows
written by Riccardo Balin
has been approved for the Department of Aerospace Engineering Sciences

_____

Kenneth Jansen

_____

John Farnsworth

Date_____

The final copy of this thesis has been examined by the signatories, and we
Find that both the content and the form meet acceptable presentation standards
Of scholarly work in the above mentioned discipline.

Balin, Riccardo (Aerospace Engineering)

The Effects of Time Step on Reynolds Averaged Navier-Stokes Simulations of High-Lift Flows

Thesis directed by Professor Kenneth Jansen

The linear finite element, time-implicit PHASTA flow solver was employed to perform Reynolds Averaged Navier-Stokes (RANS) simulations of the DLR F11 model studied for the 2nd AIAA CFD High Lift Prediction Workshop. The geometry is representative of a commercial aircraft in landing configuration, with full-span slats and Fowler flaps deployed. The effects of time and spatial resolution of the numerical computation on the predicting capability of the solver were investigated for the geometry at two angles of attack; namely 7° and 21°. At 7°, the geometry is in the linear section of the lift curve, however 21° is a post-stall stall condition for the F11 wing. A time step study was conducted with RANS and unsteady RANS simulations, as well as a grid refinement study with both uniform refinement and local, error-based adaptation.

Analysis of the results obtained from the time step study showed that at 7° angle of attack, time step does not have a significant effect on the predicting capability of the solver. However, for the F11 geometry at 21° angle of attack, time accuracy for both the transient phase and the limit cycle is important in order to avoid significant modeling errors in the solution due to the unsteady flow features present. The grid refinement study indicated that mesh refinement can be a valuable tool to improve the flow prediction, however overprediction of separation regions cannot be corrected. Furthermore, error-based, local adaptation was proved to be a more efficient approach compared uniform refinement of the entire grid.

Contents

Tables

Figures

vii

Chapter 1

Introduction

In the past decades, significant research efforts have been spent on understanding the complex features of high-lift flow fields such as the one created from a multi-element wing near stall condition. Due to their ability to generate the massive amounts of lifting force required for takeoff and landing, multi-element wings are essential for large transport aircraft. In recent years, airport noise regulations have become increasingly demanding, forcing researchers to study the flow structures created by multi-element wings and seek solutions that would reduce noise generation. Moreover, as seen by the Airbus A380 and A400M, the loading requirements of transport aircraft have been rising. Consequently, optimal design of the high lift devices is necessary for near stall operations, requiring a thorough understanding of the influence of the geometry on the flow field. In addition, active flow control has been shown [1] to be an effective solution for delaying the effects of stall on a wing, however this can only be correctly implemented once the flow is understood.

The importance of high-lift flow fields generated by multi-element wings is evident. Nevertheless, the correct simulation of these flows remains one of the major challenges in Computational Fluid Dynamics (CFD) due to their complex nature. The interaction of the various elements with each other combined with the complex features of the geometries result in a flow field characterized by strong adverse pressure gradients, regions of unsteady separated flow mixed with regions of highly accelerated strained flow, wake-boundary layer interaction, boundary layer transition, and other three-dimensional effects. In addition, proper discretization of the flow domain can also be challenging, and in some cases prohibitive given the available computational resources. For these reasons, The American Institute of Aeronautics and Astronautics (AIAA) has organized a series of workshops [2] [3] with the intent of bringing numerous research groups together in order to advance the understanding and CFD prediction capability of high-lift flow physics.

Many of the groups involved in the AIAA workshops and other groups studying high-lift flows generated by multi-element wings employed Reynolds Averages Navier-Stokes (RANS) turbulence models. These models have been showed to perform fairly well on a three-element wing for moderate angles of attack [4] [5]. However, even for

simulations performed in the liner region of the lift curve, RANS CFD codes are not able to capture some of the complicated, unsteady flow physics that generate around the wing supports, the tip of the wings and the wing-body juncture [4]. For larger angles of attack approaching stall condition, RANS simulations have not been as successful. At these conditions, the unsteady, vortical structures generated by the flap and slat supports of the three-element wings have a significant impact on the high-lift dynamics and stall dynamics of the flow field [6]. Correct modeling of these structures is a great challenge for CFD codes employing RANS turbulence models. The comparison between the experimental and numerical lift curves obtained from the 2nd AIAA CFD High Lift Prediction Workshop (HiLiftPW-2) presented in Figure 1 clearly demonstrates these challenges, especially for angles of attack near maximum lift.
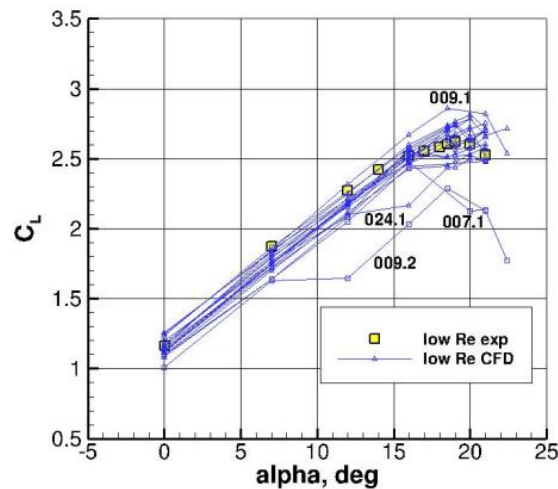
Figure 1: Comparison of the experimental and numerical lift curves for the geometry used in the HiLiftPW-2. [5]

Better prediction can be obtained transitioning to hybrid turbulence models (e.g., Detached Eddy Simulation (DES) and Delayed DES), combining RANS with Large Eddy Simulation (LES) modeling in order to resolve more of the turbulent flow structures [7]. However, the increase in the computational cost required to properly apply hybrid models is often prohibitive for large geometries. Therefore, currently there is the need to improve the predictive capability of RANS CFD codes for high-lift flows in order to satisfy the requirements of the Aerospace community. This is the motivation behind the work presented in this document. RANS simulations were run on the geometry supplied by the HiLiftPW-2, and the effects of time step size, initial conditions, and grid resolution were investigated in order to develop modeling guidelines specific to high-lift flows. Two angles of attack were considered for the geometry, one in the linear section of the lift curve where the flow is mainly attached and one in

2

the post-stall regime where massive regions of separated flow are present. The HiLiftPW-2 geometry is shown in Figure 2 and is representative of a wide-body commercial aircraft with the wing in landing configuration.

(a) Upper surface of the wing.　　　　(b) Lower Surface of the wing.
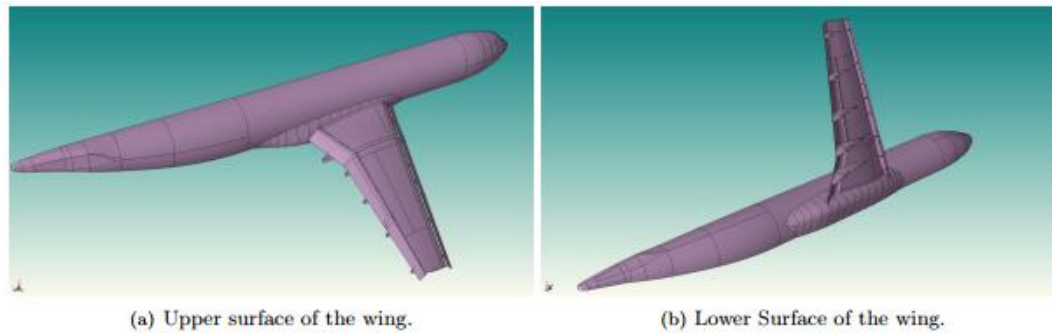
Figure 2: High-lift configuration studied in the HiLiftPW-2. [7]

This document is organized as follows. First, an overview of the Navier-Stokes solver selected to run the simulations is presented in Chapter 2, along with the flow equations being solved and method used for time integration. The RANS turbulence model employed is also outlined in Chapter 2. Chapter 3 describes the experimental geometry from which the HiLiftPW-2 model originated, as well as the wind tunnel tests performed and the data available. The chapter then presents the numerical geometry used in the simulations, the problem definition for the simulations and the meshes utilized. The fourth chapter includes the results gathered form the simulations. It is divided into two main sections, the first focuses on the time step study performed while the second is reserved to the grid refinement study. Finally, Chapter 5 offers the conclusions drawn from the work presented in the thesis and outlines the ideas for future work.

Chapter 2

Navier-Stokes Solver

2.1 PHASTA Flow Solver

The Navier-Stokes solver used for the simulations presented in this work is the highly-scalable PHASTA (Parallel Hierarchic Adaptive Stabilized Transient Analysis) flow solver. PHASTA uses a stabilized finite element method to solve both the Compressible and Incompressible Navier-Stokes equations, and performs time integration with the fully implicit generalized-α method. PHASTA has the capability of using higher order, piecewise polynomials to interpolate the solution, however the computations for this work used piecewise linear finite elements. The solver is augmented with turbulence models and level sets for two phase flows, and solves any additional equation along with the flow in a staggered approach. PHASTA is designed to work on unstructured meshes, and works best with all-tetrahedra meshes.

2.1.1 Finite Element Formulation

Given the Mach number (M = 0.175) of the high-lift flow simulated for this work, the incompressible branch of PHASTA was used. This part of the code solves the Incompressible Navier-Stokes (ICNS) partial differential equations expressed in the advective form. The system of differential equations expressed in the strong form is composed of Eq. (2.1) and Eq. (2.2),

$$u_{i,i} = 0 \tag{2.1}$$

$$u_{i,t} + u_j u_{i,j} + p_{,i} = \tau_{ij,j} + f_i \tag{2.2}$$

where u_i is the velocity vector expressed in indicial notation, p is pressure divided by density, ρ, f_i is the body force vector divided by density, and τ_{ij} is the viscous stress tensor defined in Eq. (2.3).

$$\tau_{ij} = \nu S_{ij} = \nu \left(u_{i,j} + u_{j,i} \right) \tag{2.3}$$

Einstein summation convention is used to express the governing equations, and the comma indicates differentiation.

Equations (2.1) and (2.2) create a system of four differential equations, and represent conservation of mass and momentum, respectively. Note that the differential equation specifying conservation of energy is not being solved

4

because it is assumed that the molecular viscosity of the fluid is independent of temperature changes, which in turn are assumed to be small.

At the core of the finite element method for the spatial discretization of the system of differential equations are integrals over the elements of the problem domain, therefore the system of equations is first represented in its weak (integral) form. We start by creating two function spaces of trial solutions, one, P, to contain the solutions to the fluid pressure, and the other, S, to contain the solutions to the fluid velocity. We also multiply the governing equations in Eq. (2.1) and Eq. (2.2) by two weighting functions, q and w_i, respectively, which are also part of function spaces $w_i \in W$ and $q \in P$. We then add Eq. (2.1) to Eq. (2.2) with the respective weights, while rearranging the momentum equation slightly, and integrate over the entire problem domain Ω to obtain the weak form in Eq. (2.4).

$$\int_\Omega \left[qu_{i,i} + w_i \left(u_{i,t} + u_j u_{i,j} + p_{,i} - \tau_{ij,j} - f_i \right) \right] d\Omega = 0 \tag{2.4}$$

The weak formulation of the problem states: find $p \in P$ and $u_i \in S$ for all $w_i \in W$ and $q \in P$ such that Eq. (2.4) is satisfied [8]. More details on the weak formulation of the ICNS and the function spaces may be found in reference [9].

The function spaces of the trial solutions and the weight functions defined for the weak formulation of the problem are infinite dimensional. Also, the integral in Eq. (2.4) is defined over the entire domain, meaning that is it not possible to solve analytically for most problems. Galerkin's method coupled with finite element discretization is therefore employed as a means to discretize the domain and to provide an approximation to the weak formulation. The infinite dimensional spaces are replaced by approximate, pre-established finite dimensional spaces, and the continuity, pressure and stress terms in Eq. (2.4) are integrated by parts. The Galerkin formulation of the problem reads: find find $p \in P^h$ and $u_i \in S^h$ for all $q \in P^h$ and $w_i \in W^h$ such that Eq. (2.5) is satisfied. The superscript h indicates that the function spaces are finite [8].

$$\int_\Omega \left[-q_{,i} u_i + w_i \left(u_{i,t} + u_j u_{i,j} - f_i \right) + w_{i,j} \left(\tau_{ij} - p\delta_{ij} \right) \right] d\Omega + \int_\Gamma \left[qu_i n_i - w_i \left(\tau_{ij} - p\delta_{ij} \right) n_j \right] d\Gamma = 0 \tag{2.5}$$

In Eq. (2.5), Γ is the boundary of the problem domain, n_i is the outward normal vector to Γ, and δ_{ij} is the Kroneker delta.

It is known that the Galerkin formulation is unstable for advection dominated flows. Consequently, the first integral in Eq. (2.6) is added to the left hand side of Eq. (2.5) to provide stabilization to both the momentum and continuity equation. The stabilization term performs a Streamline Upwind Petrov-Galerkin (SUPG) method on the

momentum residual and a Galerkin Least Squares (GLS) method on the continuity residual. Since the governing equations in Eq. (2.1) and Eq. (2.2) are expressed in advective form and thus not conserving momentum, a conservation restoration term is also added to the Galerkin formulation. This is the second integral in Eq. (2.6), which adds advection with its first term and performs additional stabilization with its second term. Definitions of the terms in Eq. (2.6) may be found in reference [9] and [10].

$$\sum_{e=1}^{n_{el}} \int_{\Omega^e} \left[\tau_M \left(u_j w_{i,j} + q_{,i} \right) L_i + \tau_C w_{i,i} u_{j,j} \right] d\Omega^e + \sum_{e=1}^{n_{el}} \int_{\Omega^e} \left[w_i \hat{u}_j u_{i,j} + \bar{\tau} \hat{u}_j w_{i,j} \hat{u}_k u_{i,k} \right] d\Omega^e \qquad (2.6)$$

Equation (2.6) is written as the sum over all the total number of elements, n_{el}, of integrals over the element domains Ω^e. The Galerkin formulation in Eq. (2.5) can be expressed in the same way, and when the stabilization and conservation restoration terms are included, the result is Eq. (2.7).

$$\int_{\Omega^e} \left[-q_{,i} u_i + w_i \left(u_{i,t} + u_j u_{i,j} - f_i \right) + w_{i,j} \left(\tau_{ij} - p\delta_{ij} \right) \right] d\Omega^e + \int_{\Gamma^e} \left[q u_i n_i - w_i \left(\tau_{ij} - p\delta_{ij} \right) n_j \right] d\Gamma^e$$
$$+ \sum_{e=1}^{n_{el}} \int_{\Omega^e} \left[\tau_M \left(u_j w_{i,j} + q_{,i} \right) L_i + \tau_C w_{i,i} u_{j,j} \right] d\Omega^e + \sum_{e=1}^{n_{el}} \int_{\Omega^e} \left[w_i \hat{u}_j u_{i,j} + \bar{\tau} \hat{u}_j w_{i,j} \hat{u}_k u_{i,k} \right] d\Omega^e = 0 \qquad (2.7)$$

In Eq. (2.6) and Eq. (2.7) the term L_i is used to represent the residual of the ith momentum equation, which is derived from Eq. (2.2) moving the viscous and body force terms to the left-and side thus setting the equation to zero. The term $\hat{u}_i$ is the advective velocity correction, viz

$$\hat{u}_i = -\tau_M L_i \qquad (2.8)$$

which depends on the momentum stabilization parameter defined as

$$\tau_M = \frac{\rho}{\sqrt{c_1 / \Delta t^2 + c_2 u_l g_{lj} u_j + c_3 \nu^2 g_{ij} g_{ij}}} \qquad (2.9)$$

Note that the denominator of Eq. (2.9) is the sum of the square of a CFL (Courant-Friedreichs-Lewy) time scale, and advective time scale and a diffusive time scale. The continuity and advective velocity correction stabilization parameters are as follows

$$\tau_C = \frac{1}{8\tau_M g_{ii}} \qquad (2.10)$$

$$\bar{\tau} = \frac{\tau_M}{\sqrt{L_l L_m g_{lm}}} \qquad (2.11)$$

Finally, the term $g_{ij} = \xi_{k,i} \xi_{k,j}$ is the covariant metric tensor for the mapping from global to element coordinates.

Consistent with the Galerkin method, we let the finite function spaces consist of all linear combinations of the same basis (interpolation) functions N^A, for $A=1,\ldots,n_{np}$ where n_{np} is the total number of nodal points. It follows that

6

the approximated functions spaces have dimension equal to the number of nodes in the discretized domain. In the case of linear finite elements, the basis functions are hat functions which take a value of one at node *A* and zero everywhere else. The weight functions and trial functions are then expressed as in Eq. (2.12), with the spatial derivatives defined in Eq. (2.13).

$$w_i = \sum_{A=1}^{n_{np}} N_i^A w_i^A \quad q = \sum_{A=1}^{n_{np}} N^A q^A \quad u_i = \sum_{A=1}^{n_{np}} N_i^A u_i^A \quad p = \sum_{A=1}^{n_{np}} N^A p^A \tag{2.12}$$

$$w_{i,j} = \sum_{A=1}^{n_{np}} N_{i,j}^A w_i^A \quad q_{,j} = \sum_{A=1}^{n_{np}} N_{,j}^A q^A \quad u_{i,j} = \sum_{A=1}^{n_{np}} N_{i,j}^A u_i^A \quad p_{,j} = \sum_{A=1}^{n_{np}} N_{,j}^A p^A \tag{2.13}$$

Substituting Eq. (2.12) and Eq. (2.13) into Eq. (2.7) yields a system of ordinary differential equations where the unknowns are w_i^A and q^A. Note that the integrals are evaluated by first mapping them to a parent domain, and then employing Gaussian quadrature.

2.1.2   Time Integration

The time integrator implemented in PHASTA is the generalized-α method from reference [11]. It is a predictor, multi-corrector, second-order accurate method which can be set to behave as a midpoint rule integrator, as Gear's two-step backward difference method, or anything in-between. When applied to the finite element formulation of the ICNS equations, three parameters are generated. Taylor series analysis is used to relate the three parameters, and ensuring second-order accuracy constrains two parameters leaving one free. All three parameters are then expressed in terms of the amplification factor. As a result, the free parameter of the method reduces to the amplification factor ρ_∞, used to determine the type of integrator. Midpoint rule is achieved with $\rho_\infty = 1$, while Gear's method is implemented with $\rho_\infty = 0$. PHASTA, however, can also perform the implicit, first-order accurate Backward Euler method.

2.2 Turbulence Models

In the incompressible branch of PHASTA, scalar equations, such as the ones required for turbulence modeling, are solved using the staggered approach. Consequently, the flow and the scalar are treated separately. In addition, when one set of equations is being solved, the solution from the other system is frozen. The scalar equations are discretized with linear finite elements in a manner similar to the ICNS equation described in Section 2.1, and time integration is also performed with the generalized-α method.

7

The specific staggered approach chosen for the computations in this work solved and updated the flow field twice, solved and updated the turbulence scalar field twice, and then repeated the same sequence once more before moving to the next time step. In the initial development of the code, it was established that the staggered approach offered an efficiency advantage over the fully coupled approach. Moreover, it is desirable to update the flow solution (velocity and pressure fields) before solving the turbulence model equations, which are highly dependent on velocity, to obtain faster convergence of the scalar residual. One drawback of the staggered approach is seen when the time step size is large enough for the separate time marching of the solutions to create time lag issues and slower convergence. These issues, however, were not encountered due to the fact that the flow velocity and mesh size in the boundary layers of the model forced the time step size to be small [12].

PHASTA is equipped with both RANS turbulence models, and hybrid RANS/LES turbulence models. The Spalart-Allmaras (SA) one-equation turbulence model was selected for all RANS simulations included in this report.

2.2.1   Spalart-Allmaras One-Equation Turbulence Model

The development of the Spalart-Allmaras one-equation turbulence model in 1992 was motivated by the general dissatisfaction of the turbulence models existing at the time. The central quantity of the model is the eddy viscosity v_t, thus the model is expressed in terms of a transport equation for this quantity developed from scratch. The Reynolds stresses, which result from the RANS equation, are defined according to the Boussinesq approximation in Eq. (2.14), where S_{ij} is the mean strain rate tensor $S_{ij} = \left(u_{i,j} + u_{j,i} \right)$.

$$\tau_{ij}^r = -\overline{u_i' u_j'} = v_t S_{ij} \tag{2.14}$$

Equation (2.15) is the transport equation for what is referred to as the SA-noft2 turbulence model. The noft2 term in the name indicates that the model does not include the tripping functions that were part of the original development [13], and are used to specify the location where boundary layer tripping occurs.

$$\frac{D\tilde{v}}{Dt} = c_{b1}\tilde{S}\tilde{v} + \frac{1}{\sigma}\left[\nabla \cdot \left((v + \tilde{v})\nabla \tilde{v} \right) + c_{b2}(\nabla \tilde{v})^2 \right] - c_{w1} f_w \left(\frac{\tilde{v}}{d} \right)^2 \tag{2.15}$$

Note that the solution variable is $\tilde{v}$, not the eddy viscosity. The two are equal everywhere except for in the viscous, near-wall region where they are related according to $v_t = \tilde{v} f_{v1}$, with the wall damping function

$$f_{v1} = \frac{\chi^3}{\chi^3 + c_{v1}^{\,3}} \tag{2.16}$$

and $\chi = \tilde{\nu}/\nu$. Definitions of the other damping functions and constants in Eq. (2.15) and Eq. (2.16) may be found in reference [13].

The last term on the right hand side of Eq. (2.15) is the eddy viscosity destruction term, which depends on the inverse of the square of the distance to the wall d. Consequently, the distance to the wall is the length scale of the SA model, which also appears explicitly in the equation. This feature is not present in two-equation turbulence models, where the length scale is defined implicitly from other terms. The second component of the diffusion term is $c_{b2}(\nabla\tilde{\nu})^2$, and in the model implementation in PHASTA it is grouped with the advective derivative creating a modified velocity $\tilde{u}_j = u_j - (c_{b2}/\sigma)\tilde{\nu}_{,j}$.

The SA one-equation model was developed and calibrated to perform well on aerodynamic flows [13], so wall bounded flows with nonzero pressure gradients. Because of this, along with the relative simplicity of the model equation and the boundary conditions it requires, it has become very popular in the CFD community. In fact, the majority of the participants at the HiLiftPW-1 and HiLiftPW-2 performing RANS computations employed the SA turbulence model, or a variant of it [4] [5].

Chapter 3

Geometries and Problem Definition

3.1 Experimental Geometry

The geometry used in this study is the DLR-F11 wing-body high lift configuration selected for the HiLiftPW-2. It is representative of a commercial wide-body aircraft in landing configuration, and was designed by Airbus Deutschland. The model for wind tunnel tests, however, was manufactured by DLR. The model consists of only one wing and half of the fuselage to exploit the symmetry of the geometry, and does not include horizontal or vertical stabilizers, a nacelle and a pylon. The main dimensions of the wind tunnel model are listed in Table 1, and the experimental model itself is shown in Figure 3.

Table 1: Main dimensions of the DLR-F11 experimental model. [3]

Half span [m]	1.4
Wing reference area [m^2]	0.419
Mean aerodynamic chord [m]	0.347
Aspect ratio	9.35
Taper ratio	0.3
Quarter-chord sweep [°]	30
Fuselage length [m]	3.08

Figure 3: Experimental model of the DLR-F11 wing-body high lift configuration. [3]

The high lift system of the wing includes a full-span leading edge slat with a deflection angle of 26.5° and a full-span Fowler flap deflected at 32.0° from the horizontal. The wing elements were manufactured from polished steel, while the fuselage shells are carbon fiber. The slat was attached to the main element with seven slat tracks spread fairly evenly along the span of the wing. Similarly, the flap was secured on the main element lower surface

with 5 flap tracks, which were then covered with the flap fairings seen in Figure 3. The locations of the support structures as well as those of the pressure stations are depicted in the schematic of the wing as seen from above in Figure 4. Note there are 10 pressure stations with ports on all three elements of the wing. Due to the size of the slat tracks, the pressure tube bundles had to be attached externally to the track when connecting from the slat to the main element. This arrangement is shown in Figure 5 for one of the slat tracks.
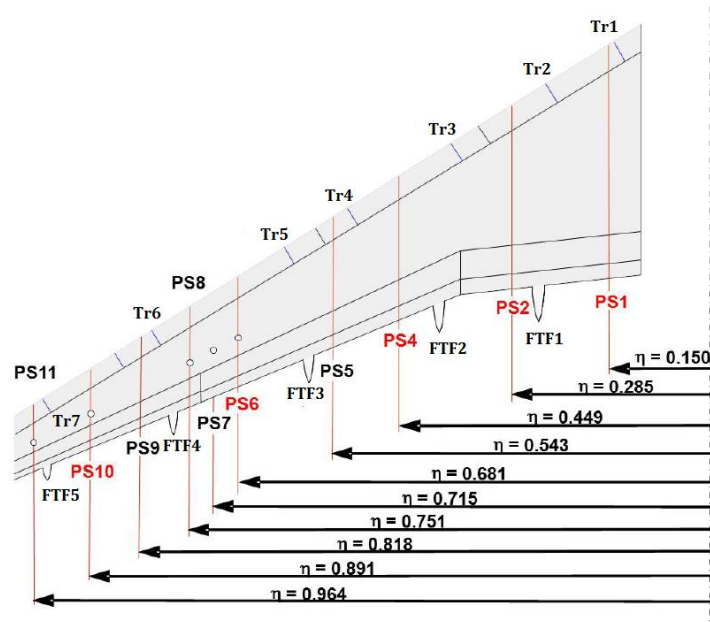
Figure 4: Schematic of the F11 wing as seen from above showing the location of the pressure stations (PS), slat tracks (Tr) and flap track fairings (FTF) relative to the symmetry plane of the geometry. [3]

Figure 5: Attachment of slat pressure tube bundles (left) and test quads (right) to a slat track in the experimental model. [3]

The wind tunnel model was tested at two separate Reynolds numbers, namely 1.35×10^6 and 15.1×10^6. The latter is representative of flight conditions, however this study focused on the low Reynolds number test because of the greater availability of experimental data for CFD validation. The test was conducted in the AIRBUS low speed wind

tunnel B-LSWT in Bremen, which has an open Eiffel-type circuit [3]. The test section is located in the return circuit, and has a length of 4.45 m and a square cross-section of 2.10 m [3]. the F11 model was attached to a turn table in the ceiling of the test section as shown in Figure 3. Note the presence of a Peniche between the fuselage and the wind tunnel wall. All experimental data available was recorded with the specific onflow conditions detailed in Table 2 and on the experimental model as described above. Moreover, the test was carried out with forced transition of the boundary layer on the nose of the fuselage only, and the boundary layer on the wing elements was allowed to develop naturally.

Table 2: Onflow conditions for the wind tunnel tests on the F11 model. [3]

Average Quantity	
Mach number, M	0.175
Reynolds number based on wing aerodynamic chord, Re_c	1.35×10^6
Onflow velocity [m/s]	60

3.1.1   Overview of Experimental Data

The experimental data available on the wind tunnel tests performed by DLR consists of force and moment coefficients, pressure coefficient measurements at the ten pressure stations along the wing, oil flow images, and more. The former two were measured for a variety of angles of attack ranging from 0° to 21°. However, the oil images were taken only for 7°, 18.5° and 21°. Of the aerodynamic forces measured in the tests, the lift is the only one that is considered in this work. The lift curve of the F11 geometry as a function of angle of attack is shown in green in Figure 6. Note that the black curve is for the F11 geometry with tube bundles attached to the slat tracks as in Figure 5. The maximum lift coefficient for this experimental model was 2.62 occurring at an angle of attack of 19°, after which stall effects occur smoothly and gradually. The linear relationship between lift and angle of attack breaks down at approximately 11°.

Given the size and the location of the slat tube bundles, the experimentalists were concerned about the aerodynamic effect these features would have on the flow and the quantities being measured during the tests [3]. For this reason, the F11 wing-body geometry was tested in the same wind tunnel at the same onflow conditions without the pressure tube bundles on the slat tracks. Only the force and moment coefficients were measured during this experiment, and the lift measurements are shown in Figure 6 as the red curve.

12
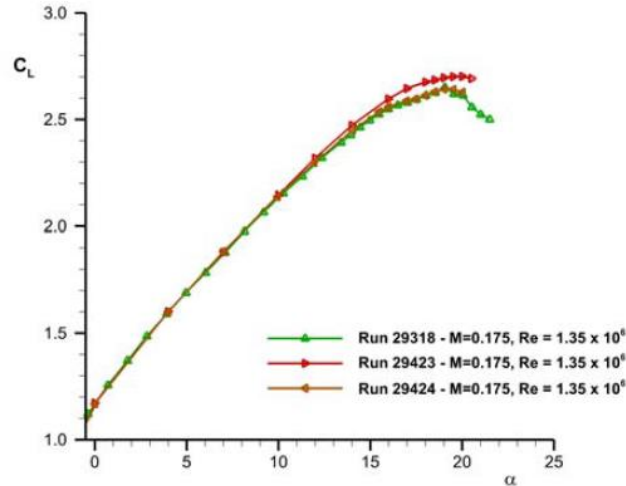
Figure 6: Lift coefficient as a function of angle of attack for the DLR F11 experimental model with tube bundles attached to the brackets (green curve), without tube bundles (red curve), and with quads (orange curve). [3]

Clearly, the tube bundles have a non-negligible effect on the measured lift at the larger angles of attack. In fact, the maximum lift coefficient of the geometry with no tube bundles is 2.71 at 20° angle of attack. At angles of attack in the linear part of the lift curve, however, the effect of the bundles is negligible. The orange curve in Figure 6 is the measured lift coefficient when the F11 geometry was run with quads that provided a similar blockage to the flow as the tube bundles, proving that the tube bundles were in fact the cause of the discrepancy between the red and the green curves. One of the quads used during the test is shown in Figure 5 on the right. These quads were used as a simplified model of the tube bundles in order to provide a similar aerodynamic effect. Note that the lift coefficient data, pressure coefficient data, and oil flow images made available were obtained from tests on the geometry with the tube bundles on the slat tracks. The only data available for the experimental geometry with no tube bundles or no quads are plots of the force and moment coefficients, such as Figure 6.

3.2 Numerical Geometry and Problem Setup

In order to accurately represent the wind tunnel experiments, the Computed Aided Design (CAD) model used for this work was provided directly from DLR for the HiLiftPW-2. Three CAD models of increasing complexity were available to participants of the HiLiftPW-2. The first had no slat tracks or flap track fairings, therefore had the slat and the flap elements floating in free space connected only to the fuselage. The second version had slat tracks and flap track fairings but no tube bundles, while the last included the bundles as well. The second CAD model was selected to provide a compromise between fidelity to the wind tunnel tests and meshing complexity. Figure 7 shows

13

the CAD model considered as seen from above and below. Note that the CAD model provided by DLR is a representation of the experimental model, and therefore simply includes the wing-body geometry. Note the presence of the five flap track fairings and the seven slat tracks to connect the high lift devices to the main element. In the model, the x axis points in the direction of the incoming flow over the wing, therefore parallel to the symmetry plane of the geometry. The y axis points outboard from the root of the wing to the tip and is perpendicular to the x axis. Finally, the z axis points up to complete the Cartesian system.

A CAD representation of the fluid volume was then constructed from the CAD model of the aircraft. This is a solid box with the wing and fuselage geometry subtracted in the Boolean sense from it. The symmetry plane of the aircraft is aligned with one of the longest faces of the volume, and the aircraft geometry extends towards the opposite face creating a cavity, as seen in Figure 8. The position and orientation of the aircraft cavity defines the inflow plane upstream of the wing-body (the onflow velocity is in the positive x direction), the outflow plane downstream of the wing-body, the side walls, and the top and bottom walls. The box was designed with a length of 15.64 m along the x axis, a width of 2.10 m along the y axis, and a height of 2.10 m along the z axis. Note that the width and height of the computational fluid volume match the cross-sectional dimensions of the wind tunnel test section. This was purposefully done to model the F11 geometry in the test case of the wind tunnel. More specifically, the inclusion of the test section walls around the aircraft geometry, serves to model the redirection of the velocity vectors due to the walls, and not have the aircraft in a free-flight condition. The length of the fluid volume, however, is much longer than the test section of the wind tunnel. A distance of approximately 4.6 m is present between the inflow surface and the nose of the fuselage, and a distance of approximately 7.8 m exists between the tail of the fuselage and the outflow plane. These distances were deemed sufficient to ensure that most of the effects of the vortices shed downstream by the geometry could be captured, particularly those of the wing-tip vortex which is expected to be fairly strong given the significant loading on the wing. Moreover, enough distance was necessary in front of the aircraft to make the induced effects of the vortices on the velocity field are negligible at the inflow plane.

14
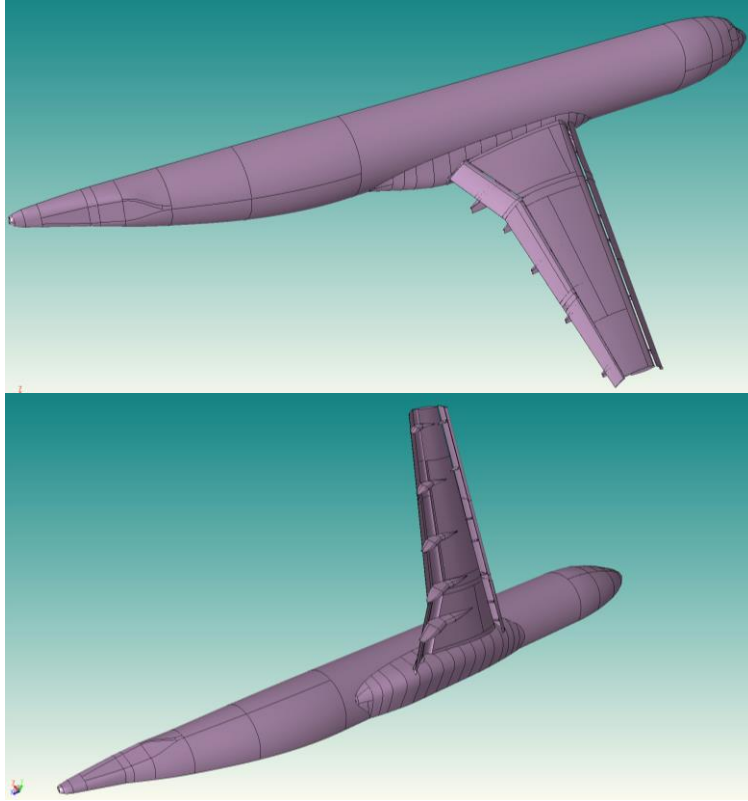
Figure 7: Upper (top) and lower (bottom) views of the CAD model of the F11 wing-body configuration used for CFD simulations.
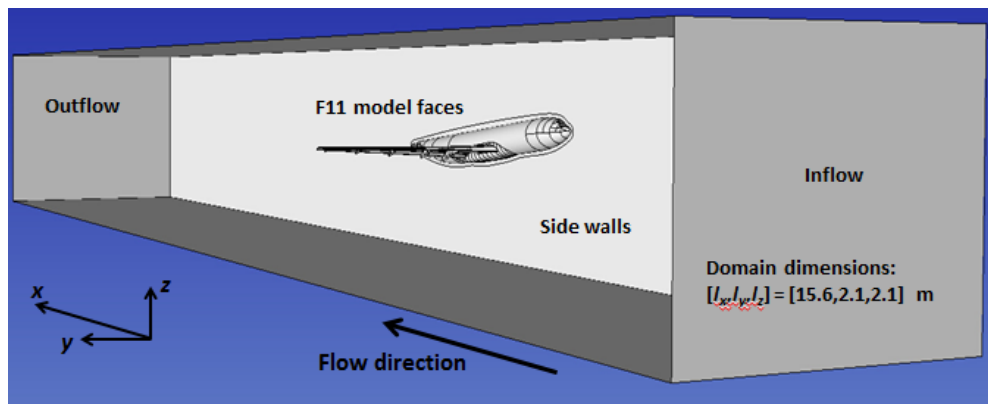
Figure 8: Schematic of the fluid volume designed for the CFD simulations.

3.2.1 Boundary Conditions and Initial Conditions

The Mach number of the F11 simulation puts the flow modeled well within the domain of the incompressible assumption. As outlined in Chapter 2, the incompressible branch of PHASTA was used to solve the flow and turbulence scalar equations, consequently the boundary and initial conditions implemented to define the problem

15

correspond to those of incompressible flow. Note that temperature is not being solved for, so this variable does not appear in any of the boundary or initial conditions.

Starting with the flow variables, at the inflow plane, which is the face of the fluid volume labeled in Figure 8, the boundary condition specified is the velocity vector. In order to simulate the conditions present in the wind tunnel experiments, the velocity vector was specified to have a magnitude of 60 m/s and to be aligned with the x direction. The outflow plane is assigned to have natural pressure, meaning that the pressure flux is zero. In addition, the traction vector is set to zero on this face to signify that there are no viscous stresses. On the surface of the F11 wing-body model, the velocity is set to zero to implement the no-slip boundary condition. On the side, top and bottom walls of the fluid volume, the trivial no penetration boundary condition is set by specifying one component of velocity to be zero. The second condition enforced was a zero traction vector, thus modeling the walls as inviscid.

The RANS turbulence model in PHASTA is the Spalart-Allmaras model outlined in Chapter 2. This is a one-equation model based on the eddy viscosity. Consequently, it is necessary to specify the value of this scalar at the computational boundaries as well. On the fuselage and wing faces, the eddy viscosity is set strongly to zero, while on all other faces, with the exception of the inflow, a weak boundary condition of zero flux is enforced. At the inflow, the eddy viscosity is set to the desired free stream value, thus setting the desired free stream turbulence level. To match the level of turbulence to the one experienced during the wind tunnel tests, a value of three times as large as the molecular viscosity was suggested to the HiLiftPW-2 participants. At room temperature, the molecular viscosity of air is approximately 1.8×10^{-5} kg·m^{-1}s^{-1}, making the free stream value of the SA scalar 5.4×10^{-5} kg·m^{-1}s^{-1}. The boundary conditions implemented are summarized in Table 3.

All simulations were initialized from the standard zero, plug-flow initial conditions. Pressure was set to zero al all nodes, while the velocity was initialized to have a negligible component in the x direction (a value of 1×10^{-8} m/s was enforced) in order to avoid division by zero in the PHASTA code. The turbulence scalar was initialized at the free stream turbulence value. These parameters are summarized in table 4.

Table 3: Boundary conditions enforced on the computational fluid domain.

Model Face	
Inflow	- Flow velocity at 60 m/s along *x* direction - SA scalar set to 5.4×10^{-5} kg·m^{-1}s^{-1}
Outflow	- Natural pressure, zero pressure flux - Zero SA scalar flux - Zero traction vector, inviscid surface
F11 model faces	- Zero velocity, no-slip wall - Zero SA scalar
Side, top, bottom walls	- No penetration - Zero SA scalar flux - Zero traction vector, inviscid surface

Table 4: Initial conditions enforced on the solution variables.

Parameter	
Pressure	Zero
Velocity	Plug flow, 1×10^{-8} m/s in the x direction
SA scalar	5.4×10^{-5} kg·m^{-1}s^{-1}

The selection of the boundary conditions for the side, top and bottom walls deserve a more detailed motivation. Two boundary conditions were set on these model faces. The first, setting a fluid velocity component to zero, is consistent with the no penetration condition for a solid non-permeable wall and is necessary in order to model those faces as the walls of the wind tunnel. The second condition is representative of an inviscid wall, where the fluid is allowed to have a non-zero velocity at the surface. This boundary condition is of course not physical because the wind tunnel walls are viscid and thus have boundary layers on them. During the tests, the boundary layers do not directly affect the flow over the experimental geometry due to the fact that the fuselage is mounted on a Peniche and the wing is far from the walls. However, there are secondary effects on the flow created by the boundary layer growth along the tunnel walls. As the momentum thickness of the boundary layer grows, the cross-sectional area that the primary flow sees is reduced. From inviscid flow theory it is known that for a constant mass flow, a reduction in cross-sectional area corresponds to an increase in the velocity of the fluid, resulting also in a drop in pressure. The boundary layers in the wind tunnel, therefore, induce streamwise velocity and pressure gradients. In the overview of the experimental data (ref) there is no reference of these gradients being accounted for, instead the data is provided as measured during the tests.

Due to the inviscid wall boundary condition, these gradients are not modeled in the CFD simulations. Modeling of these gradients would require changing the boundary conditions to no-slip surfaces, followed by generating a boundary layer mesh. However, these modifications are too computational expensive because of the significant

17

increase in mesh size. Another alternative is to estimate the momentum thickness of the boundary layer on the wind tunnel walls as a function of streamwise position and taper the walls of the fluid volume by the same amount while maintaining the slip boundary condition. Given other more significant modeling assumptions involved in the numerical problem solved, the most significant of which is the lack of pressure tube bundles, it was determined that the secondary effects produced of the gradients were small enough to be neglected.

3.3 Meshes

The The initial mesh for the fluid volume used in this study was generated with the commercial meshing package called BLMesher provided by Simmetrix Inc [14]. The mesh is unstructured in nature, with a mixture of wedge and tetrahedron shaped elements in order to comply with the PHASTA flow solver. Due to the no slip boundary conditions enforced on the faces of the fluid volume appertaining to the F11 geometry, a boundary layer mesh is required. In addition, due to the variety of scales of the model features, and due to the extended onflow and downstream regions, the surface elements of the mesh vary quite significantly in size.

The design of the mesh came from the experience gained during the participation to the HiLiftPW-2. On the upper surfaces of the slat, main element, and flap the mesh elements were set to be a size of 6.2×10^{-3} m. Closer to the leading and trailing edges of these surfaces, however, the mesh elements were on the order of 4×10^{-4} m. The same size was used to design the surface grid on the small features of the geometry, such as the slat tracks. The first point off of the wall was designed to be a distance of 2.0×10^{-6} m from the surface for every face that required a boundary layer mesh. The boundary layer growth factor was selected to be 1.27, meaning that the height of an element in the layer was a factor of 1.27 larger than the height of the element below it. According to reference [15], the gridding guidelines for a boundary layer to be simulated using RANS are that the first point off the wall must have a y^+ value of 2 or less, and that the growth factor of the boundary layer elements should be around 1.25. The first requirement is enforced to ensure accurate representation of the viscous sublayer, while the second is enforces sufficient resolution of the buffer and log layers. An *a posteriori* check of the boundary layer design performed on the mesh for the geometry at 21° angle of attack indicated that the y^+ values at the first point off of the wall satisfy the guideline value, and are actually of the order of $y^+ = 1$ or less. The results to this analysis are presented in Figure 9. The initial mesh is therefore capable of predicting the inner boundary layer accurately. The boundary layer height was designed to be from 5.0×10^{-4} m to 5.0×10^{-3} m depending on the model face. A check similar as the one in

Figure 9 was performed to ensure that the predicted velocity boundary layer was located within the boundary layer mesh. Note finally that the boundary layer mesh generated by the BLMesher tool is composed of anisotropic, wedge-shaped elements. These are however tetrahedronized before running PHASTA.
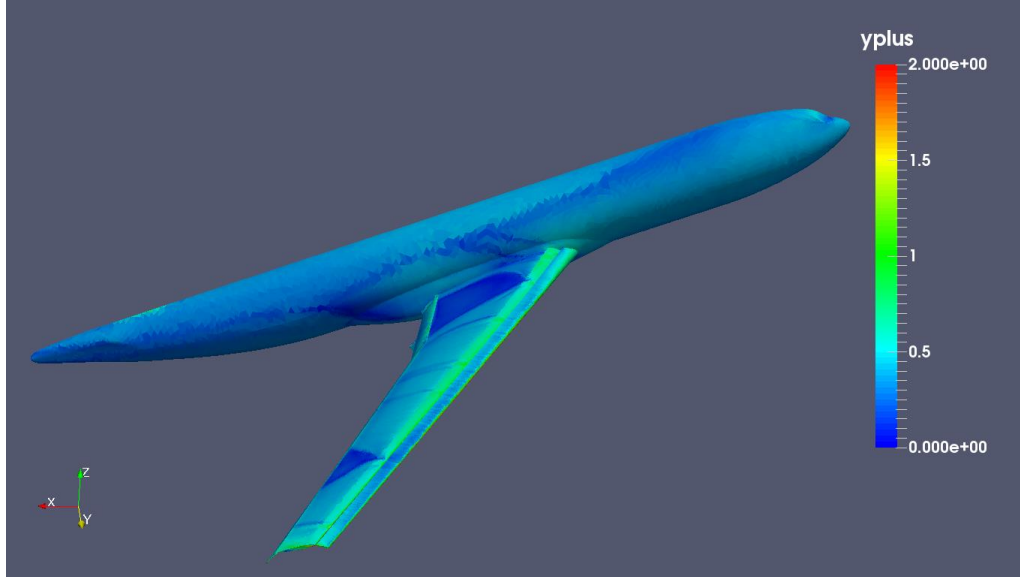

Figure 9: y^+ values at the first point off of the wall for the geometry at 21° angle of attack.

Outside of the boundary layer mesh, the rest of the fluid volume is filled with isotropic, tetrahedron-shaped elements. In the far field away from the wing, as shown in Figure 10, these elements have a size of 0.2 m. However, in the proximity of the wing the size drops to 0.035 m. Note in addition that curvature based refinement was applied to the initial mesh in order to represent the curved surfaces of the model more accurately, and in order to increase the resolution in regions where large gradients exist. This initial mesh is henceforth called A0, and can be observed in images a) and c) of Figure 11. As a reference for comparison with other meshes, before tetrahedronization the A0 mesh had a total of number of elements of approximately 75 M.

For the mesh refinement study discussed in Chapter 4, two meshes were generated with higher resolution. The first mesh, henceforth called A0-URNN, is a uniform refinement of every triangular face in the fluid domain, but not of the quadrilateral faces of the wedge-shaped elements within the boundary layer. Note this is equivalent to splitting all the edges of the mesh elements, except the edges that are aligned roughly with the normal direction to the surfaces, (e.g., URNN stands for uniform refinement non-normal). For a two-dimensional, triangular mesh, this process would increase the total number of elements by a factor of 4. Note that this refinement technique does not take into consideration the flow solution and is uniform throughout the whole domain. Figure 11 shows a

19

comparison between the A0 and the A0-URNN meshes at different locations on the F11 wing. Uniform refinement of A0 increased the number of elements to 470 M, a factor of 6 larger.

0.035 m

0.2 m
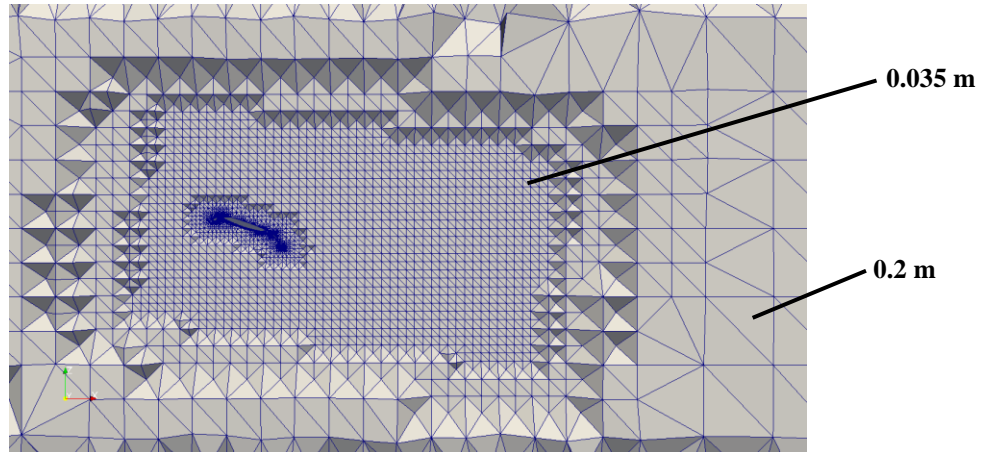
Figure 10: Slice of volume mesh around the F11 wing.

A second refinement strategy was adopted and tested in this work, namely error-based, local refinement. Contrary to uniform refinement, this technique uses information from the solution to select which sections of the mesh are in need of refinement, and which sections have already sufficient resolution. The error indicator selected is a combination of the root mean square of the velocity and the residual of the partial differential equations being solved. Therefore, this error measure identifies the regions in the mesh where the residual is large and convergence of the solution was not achieved well, and regions with large fluctuations in the velocity. Figure 12 shows the isosurface of the error indicator after a RANS simulation on the geometry at 7° angle of attack. The regions of the surface mesh enclosed by the error isosurface are those selected for refinement, the rest of the surface mesh is not altered. The refinement occurs in the same way as the uniform refinement, with every edge of the surface only being split in half. Note that local refinement was only performed for the geometry at 7° angle of attack, generating a mesh of 223 M elements henceforth named A1. Note the smaller number of elements (approximately half) of A1 compared to A0-URNN.
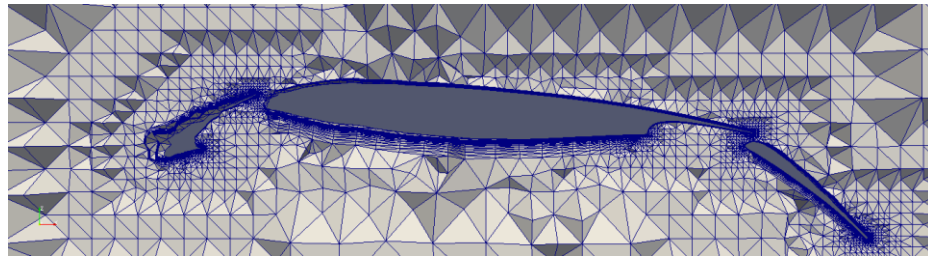
a) Wing slice of A0 mesh
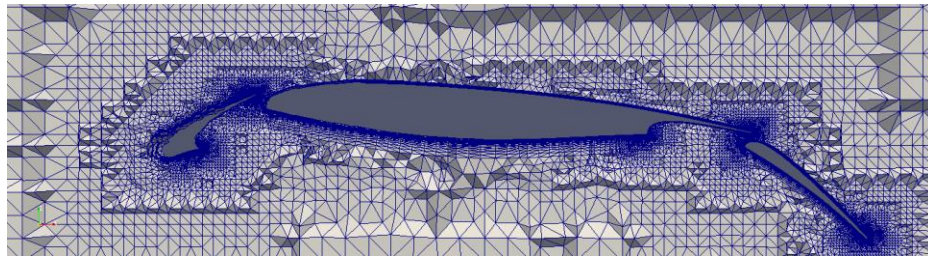
b) Wing slice of A0-URNN mesh
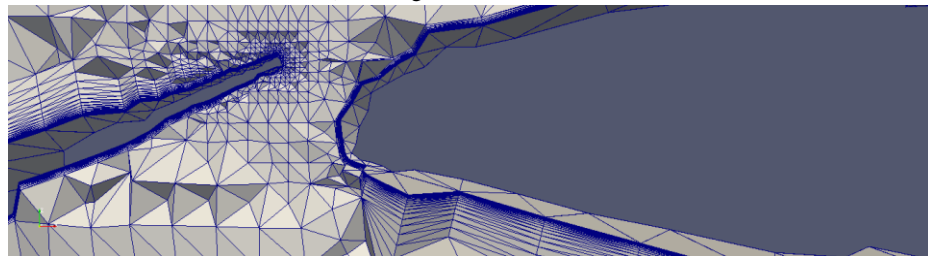
c) Slat-main element gap of A0 mesh

d) Slat-main element gap of A0-URNN mesh

Figure 11: Mesh slices around F11 wing for the A0 and A0-URNN meshes.

**Figure 12: Isosurface of the error indicator used for the local refinement on the A0 mesh with the geometry at 7°
angle of attack.**

21

Chapter 4

Time Step and Grid Refinement Studies

4.1 Time Step Study

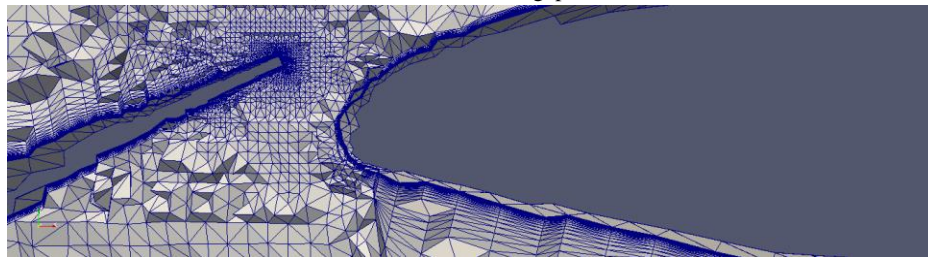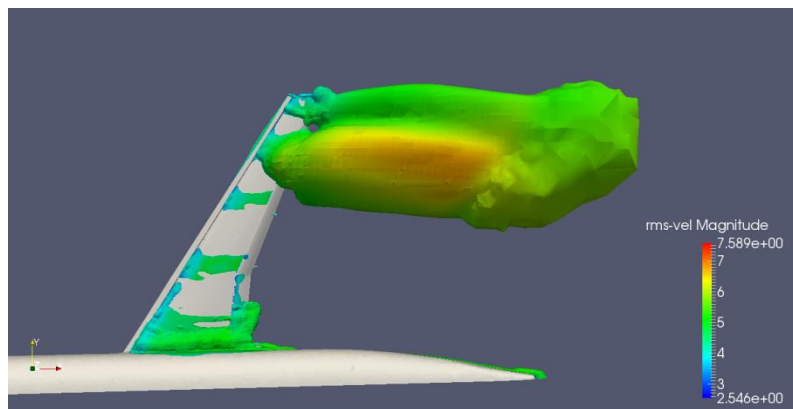It is common in the CFD community to model high-lift flows with RANS turbulence models seeking a steady-state solution of the flow field. In addition, the initial transient response of the flow as it naturally deviates from the initial conditions is often flushed out employing a large time step size. In most cases, steady state at the large time step is achieved by an adequate reduction of the nonlinear residual and of the solution delta. In this situation, solvers are designed to eliminate the unsteadiness to achieve this large time step, steady state convergence. This approach is appropriate when there is no unsteadiness in the mean flow equations and all unsteadiness is at time scales captured by the turbulence modeling averaging process. It is questionable in situations where there is low frequency unsteadiness (large scale shedding) at time scales far slower than the turbulence (e.g., vortex shedding behind a bluff body [16]. In these situations, for the sake of computational efficiency, it may be interesting to consider a progressive reduction of the time step to determine if resolution of these low frequencies alters the solution time average. This approach is also attractive for simulations with DES and DDES models, which take a RANS solution as an initial condition. The restrictions created by the time step and the resolution needed to accurately perform LES forces the saving of resources, flushing transients and pushing to a steady state. The work presented here demonstrates how these steps can lead to significant modeling errors and erroneous predictions of the flow features in cases where hysteresis and mean unsteadiness lead to solutions that are dependent on the time step history.

There are two main approaches to setting the initial conditions of numerical simulations of high-lift flows. The first approach uses the flow solution from a smaller angle of attack as the initial condition. This requires multiple simulations to be run on multiple meshes, especially if the problem of interest is set at a large angle of attack. Moreover, this first approach requires the solution that is to be used as initial condition to be accurate and not present major modeling flaws. The second approach sets zero initial conditions, regardless of the angle of attack of the geometry. The work being presented here was carried out using solely the second approach. This was done because only two angles of attack were considered for the DLR F11 geometry, namely 7° and 21°, thus the first

approach would have not been practical from both a time and computing cost perspective. Consequently, the conclusions drawn in this report are mostly applicable to simulations starting from zero initial conditions.

The two angles of attack selected for this work are representative of distinct sections of the lifting profile of the F11 wing shown in Figure 6. For the Reynolds number considered in the simulations (Re=1.35×10^6), at 7° the geometry is approximately at the center of the linear section of the lift curve, while at 21° the geometry is in a post-stall, post-maximum lift condition. The effects of time step size are therefore investigated for both a largely-attached high-lift flow field and a flow field with massive regions of separated flow.

Finally, recall that the CAD model of the F11 configuration used for the numerical simulations only includes the slat tracks and the flap fairings, however it does not include the pressure tube bundles attached on the outside of the tracks. Figure 6 clearly shows that at large angles of attack, the blocking effect of the tubes has an important influence on the lift of the experimental model. In addition, the shape of the lift curve at stall and the angle of attack at maximum lift are also modified by the absence of the tubes. These differences suggest that the structures responsible for the stall of the wing might not be the same for the configurations with and without bundles. Unfortunately, the oil flow images and the pressure coefficient data obtained from the wind tunnel tests are available only for the model with the tube bundles. Therefore, validating the actual differences in the stall mechanism is not possible. In addition, when comparing the simulation results for the numerical model at 21° angle of attack to the experiments, a note of caution must be taken in that the two results might not be supposed to match exactly. Nevertheless, given the lack of knowledge of the flow without tube bundles on the slat tracks, it will be assumed that the stall mechanism and the flow structures at 21° are similar for both configurations.

4.1.1   7° Angle of Attack

The time step investigation for the high-lift flow generated by the F11 geometry at a 7° angle of attack was carried out on the initial A0 mesh starting from zero initial conditions. Two time step sizes were selected; $\Delta t = 6.25\times10^{-3}$ s and $\Delta t = 0.25\times10^{-3}$ s. The former qualifies as regular RANS modeling, while the latter qualifies as unsteady RANS (URANS) modeling. URANS modeling differs from RANS in that it attempts to resolve the fluctuations in the mean quantities which are not associated with turbulence. Therefore, the turbulence is modeled in the same way, however Δt is reduced with the intent to capture large scale fluctuations in the mean flow, such as the vortex shedding behind a bluff body in crossflow [16]. Due to the nature of the geometry being studied, even at small

23

angles of attack the flow around the wing is not steady. In particular, the slat tracks and the flap fairings are some of the largest sources of unsteadiness, creating vortical structures that then interact with the boundary layers on the main element and flap. For this reason, it is important to understand whether the resolution of such unsteady phenomena has an effect on the predicting capability of the RANS model.

The effects of the time step size on the transient phase of the solution are seen by the lift force coefficient histories of the two simulations performed shown in Figure 13. For the RANS case, the limit cycle of the solution was obtained after approximately 50 time steps starting from zero initial conditions. In this case, the transient phase was flushed out in order to reach the steady RANS solution for this problem with a few iterations. For the URANS case, approximately 600 time steps were required, meaning that the transient phase was modeled more accurately in time. Note that while the transient phases differ, the limit cycles reach almost identical steady solutions, which overestimate the experimental lift coefficient by approximately 3.5%. Recall from Figure 6 that at 7° angle of attack, the effect of the tube bundles on the slat tracks is negligible, thus the available experimental data (lift coefficient, pressure coefficient and oil flow images) can be compared to the numerical results with confidence. The force histories also suggest that there are no large unsteady features in the flow field, since, even with the smaller time step, the limit cycle of the solution is a constant flat curve with no perturbations.
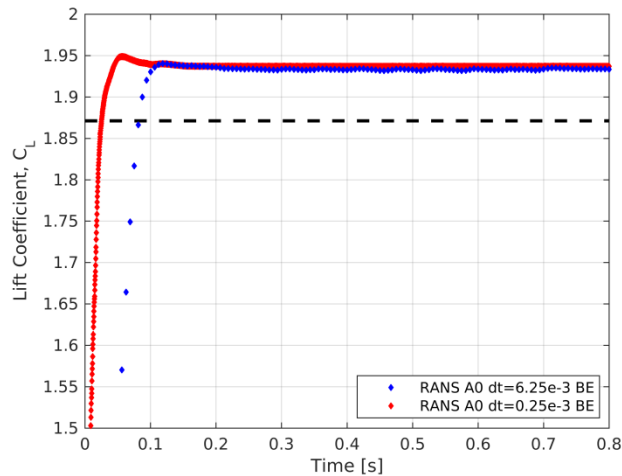
Figure 13: Lift force histories of the RANS and URANS simulations performed for the time step study on the A0 mesh at 7°. Black dashed line is the experimental value.

The pressure coefficient at different spanwise locations (Figure 4 in Chapter 3) was computed for both the RANS and the URANS simulations. It was noticed that the resulting plots were almost identical for the two time step sizes, which is not surprising given the similarity in the lift coefficients. Figure 14 shows C_p plots at four spanwise locations. It is clear that at all locations the results for the two Δt are almost identical. Note that the legends

24

in the figures have the label BE to indicate that these simulations were run with the first-order accurate, implicit Backward Euler time integrator.
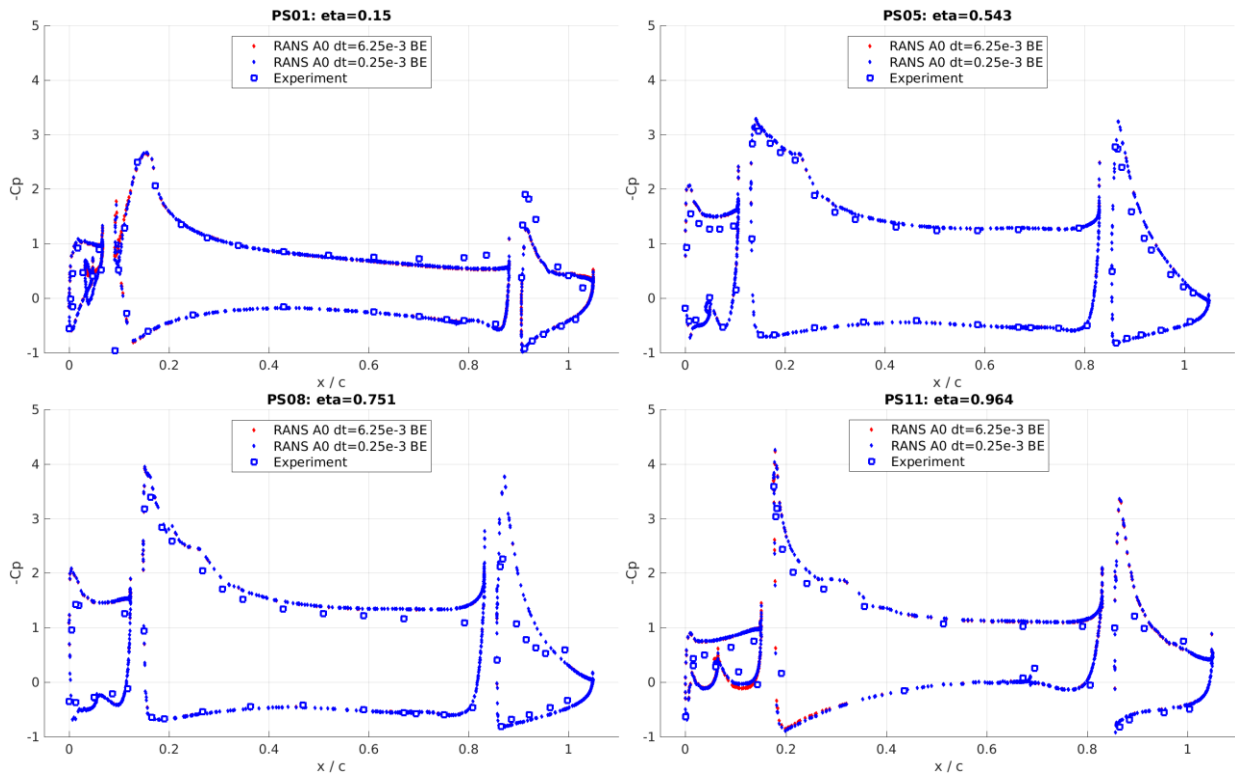
Figure 14: Pressure coefficient at different spanwise locations on the wing for RANS and URANS simulation on the A0 mesh at 7°.

The pressure coefficient plots combined with the lift force histories show that for an angle of attack of 7°, URANS simulations do not provide an advantage in terms of predicting capability. It is therefore possible in this case to start from a zero initial condition, flush the transient solution with a relatively large time step and reach a steady state solution with an inexpensive first order accurate integrator. It is worth noting that of the four pressure stations shown in Figure 14, PS1, PS8 and PS11 are the three locations where the numerical results have the largest deviation from the experimental results. All other pressure stations show an agreement with the experimental data very similar to that seen at PS5. The RANS simulation was therefore capable of predicting the high-lift flow field fairly well on the initial mesh.

Figure 15: Isosurface of the Q-criterion, Q = 1.0×10⁶, around PS1 for RANS simulation on A0 at 7° angle of attack.

In order to understand what flow features caused the shortcomings of the numerical prediction at the three pressure stations in Figure 14, the flow was visualized using Paraview [17]. At PS1 near the root, the pressure on the suction surface of the main element starts to increase (Figure 14 plots have $-C_p$ on the vertical axis) at approximately 2/3 of its chord, and keeps incre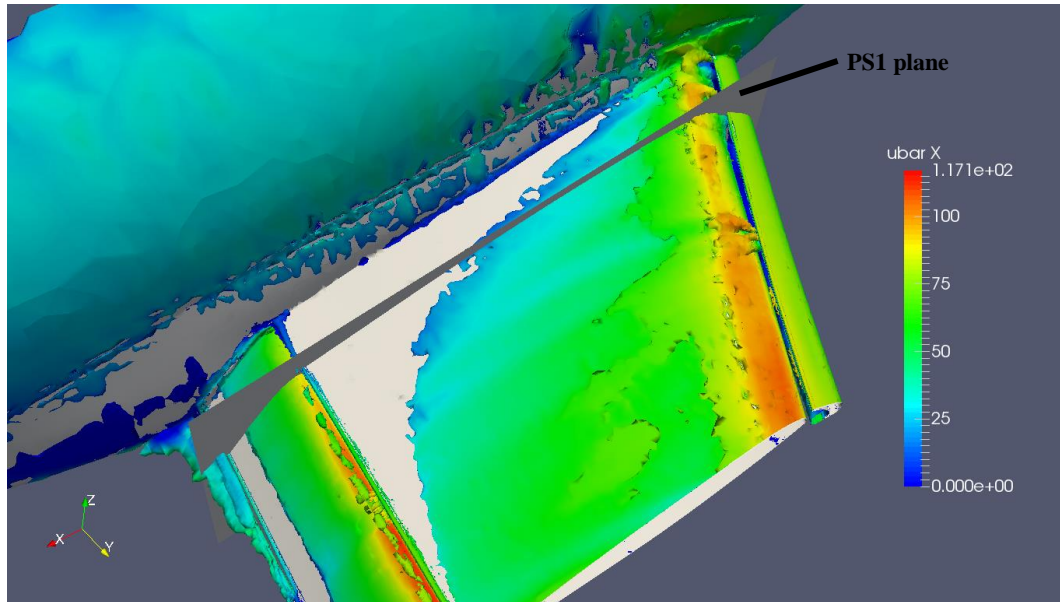asing until the trailing edge. The suction peak on the flap is also significantly underestimated. This increase in pressure suggests that the simulation predicts a region of massively separated flow that covers most of the main element at PS1. Figure 15 shows an isosurface of the Q-criterion at a value of 1.0×10^6 in the root section of the wing. The isosurface is colored by the longitudinal velocity, and the plane corresponding to PS1 is shown. The image shows that there is a region of low vorticity close to the surface of the wing characterized by small longitudinal velocity. Since the vorticity levels for a separated boundary layer are smaller than for an attached one, the region where the isosurface disappears is a separation zone. In addition, separated flow is characterized by smaller velocity in the streamwise direction, and this feature is evident in Figure 15. It can be seen that it originates at the wing-body juncture by the leading edge of the main element and extends all the way to the flap along the juncture. It also tapers away from the root of the wing due to the spanwise pressure gradient on the upper surface of the wing. Moreover, it is possible to see that the separated flow region crosses the plane of PS1 at approximately 2/3 of the chord of the main element, coinciding with the location where the pressure coefficient increased relative to the experiment. From Figure 16, however, it is clear that the size of this region predicted by the simulation is significantly larger than what was seen in the wind tunnel experiment at the same

angle of attack. In the experiment, the root vortex also originates at the wing-body juncture by the leading edge of the main element, however it reaches the plane of PS1 only at the trailing edge of the main element. Therefore, there is no massively separated flow at PS1 according to the experiment.
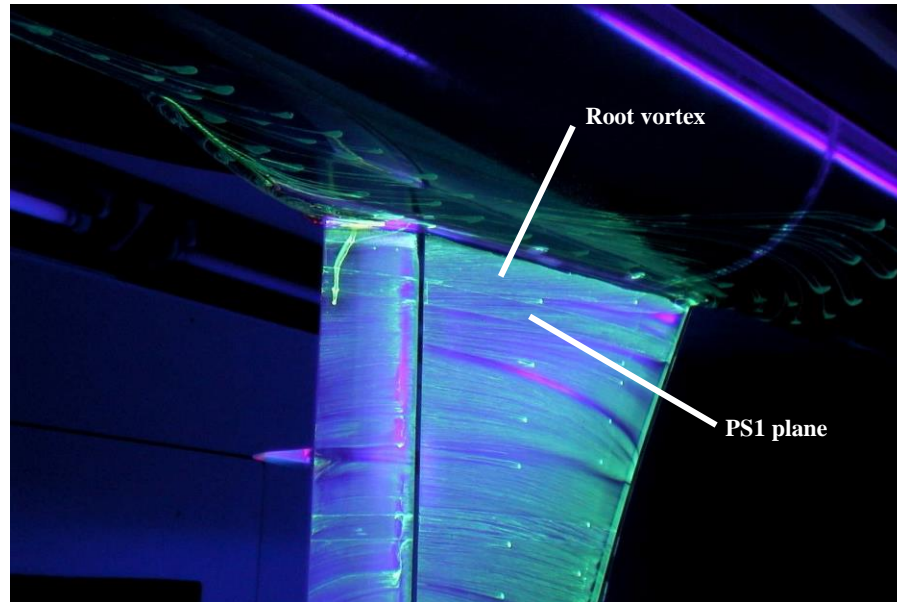

Figure 16: Oil flow image of the wing root obtained during the wind tunnel experiment on the F11 geometry at 7° angle of attack.

At PS8, the pressure coefficient profile indicates a scenario opposite of what was seen for PS1. Figure 14 shows that the pressure on the trailing edge of the main element and on the flap is greatly underestimated at this location. The experimental pressure data suggests that there is massive separation on the flap as seen by the flattening of the pressure coefficient towards the trailing edge. In addition, a region of retarded flow is also present on the trailing edge of the main element as indicated by the pressure recovery at the rightmost data point. Figure 17 supports this statement showing how massive separation (red region in the figure) occurs on the flap just outboard of PS8. This separation appears to be caused by the vortical structures generated at the flap fairing located under the wing at same spanwise location. The RANS solution presents the same structures, however their size are not accurately predicted. Figure 18 shows a contour of the average longitudinal x velocity at a value of 30 m/s, colored by the average eddy viscosity. Two vortical structures of higher eddy viscosity clearly originate from the edges of the flap fairing, in-between which there is a region of low-energy fluid coming from the upper surface of the fairing, where fluid is entrained. This low-energy fluid is more susceptible to the adverse pressure gradient on the flap and thus separates. While the correct flow structures are predicted by RANS, the volume of the separated region is underestimated and does not intersect the PS8 plane, thus accounting for the difference in the numerical and experimental pressure.

27
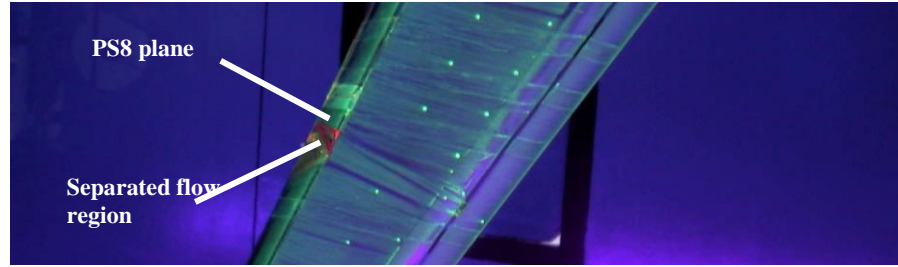
Figure 17: Oil flow image of the wing around PS8 obtained during the wind tunnel experiment on the F11 geometry at 7° angle of attack.
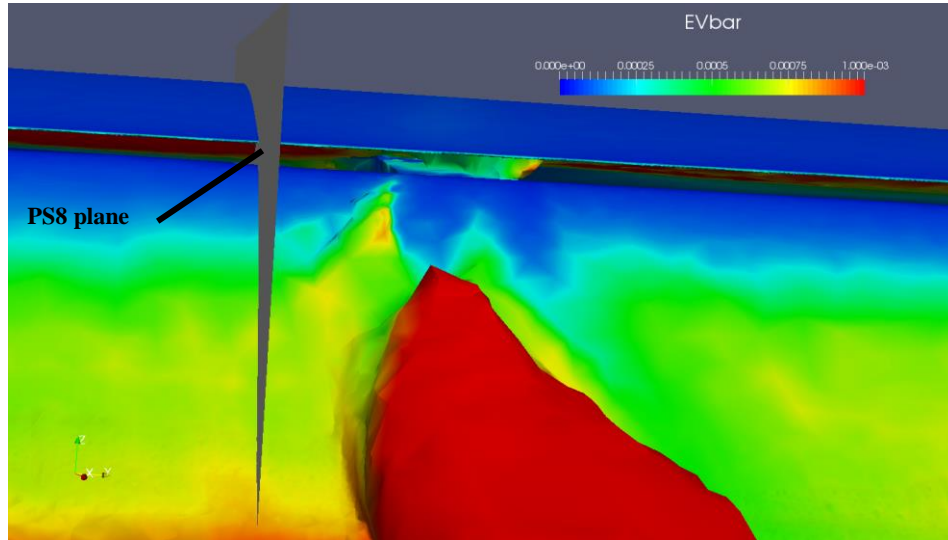
Figure 18: Isosurface of longitudinal velocity u_x = 30 m/s, around PS8 for RANS simulation on A0 at 7° angle of attack.

The disagreement between the RANS simulations on A0 and the experimental data at PS11 presented in Figure 14 is attributed to a similar cause as the one seen for PS8. As seen from Figure 4 in Chapter 3, PS11 is located slightly outboard of the fifth flap fairing, which causes a separation region on the flap. RANS predicts this region to be smaller than seen from the wind tunnel oil flow images, and therefore not affecting the pressure at PS11 in the correct manner.

While some modeling errors are present in the numerical solution, at 7° angle of attack, the transient phase of the simulation of this high-lift flow does not seem to be affected by time step in a significant way. Note also that the simulations performed for this study were carried out on the initial A0 mesh, the effects of grid refinement are shown later in this Chapter.

4.1.2 21° Angle of Attack

For the DLR F11 geometry at 21° angle of attack, three different time steps were selected. A RANS simulation was performed with a time step size $\Delta t = 6.25 \times 10^{-3}$ s using the first-order accurate Backward Euler time integrator in

order to push to a steady RANS solution in a small number of iterations. A URANS simulation was performed with $\Delta t = 0.25 \times 10^{-3}$ s and Backward Euler, and a second URANS simulation was run with $\Delta t = 5.0 \times 10^{-5}$ s using the second-order accurate generalized-α method. These three set of parameters were chosen to identify the modeling errors associated with pushing RANS to a steady solution flushing the transient, as well as those associated with performing URANS while not having a time accurate integration method. Note that all simulations run for this time step investigation used zero initial conditions and ran on the A0 mesh.

The effects of time accuracy for RANS simulations of the F11 wing at 21° angle of attack can be exemplified by the lift force coefficient histories. Figure 19 shows the computed lift coefficient for the three simulations as a function of physical time. For the RANS case (blue curve), the limit cycle of the solution is reached in approximately 50 time steps, similarly to the RANS simulation on the 7° mesh, but slower than the other cases in terms of physical time. Again, with a time step size of $\Delta t = 6.25 \times 10^{-3}$ s, the transient phase is flushed to obtain the steady RANS solution quickly. Notice, however, that differently from the simulations on the 7° mesh, the limit cycle of the lift coefficient solution does present some small perturbations. These perturbations are caused by the unstable features in the flow, which due to their size have a visible impact on the total lift. For the URANS simulations, the limit cycle of the solution is achieved at approximately 1500 time steps for the case with $\Delta t = 6.25 \times 10^{-3}$ s (green curve), and at 6,000 time steps for $\Delta t = 5.0 \times 10^{-5}$ s (red curve). Note that due to the increased time accuracy of URANS, the perturbations in the lift coefficient caused by the unsteady flow features are indeed captured, increasing in magnitude as the time step is reduced. In addition, the difference in the prediction of the lift coefficient for the three simulations is evident, suggesting that time step does have a significant impact on the limit cycle of the simulation at this angle of attack. The experimental lift coefficient extrapolated from the red curve in Figure 6 for the geometry with no tube bundles or quads on the slat tracks is shown in Figure 19 as the dashed line and has a value of approximately 2.67. The computed lift coefficients for the three simulations run in the first time step study are 2.32, 2.49, 2.67 for $\Delta t = 6.25 \times 10^{-3}$ s, $\Delta t = 0.25 \times 10^{-3}$ s and $\Delta t = 5.0 \times 10^{-5}$ s, respectively. URANS with generalized-α gave and the smallest time step therefore appears to be able to predict the proper lift coefficient. The other two cases underpredicted the lift by up to 13% for the RANS case.
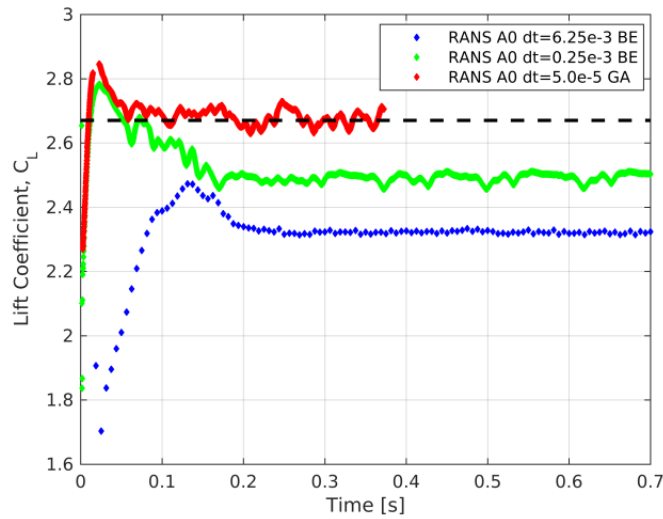
Figure 19: Lift force histories of the RANS and URANS simulations performed for the time step study on the A0 mesh at 21°. Black dashed line is the experimental value extrapolated from the red curve in Figure 6 for the geometry with no tube bundles or quads on the slat tracks.

Figure 20 shows the computed pressure coefficients at several spanwise locations along the wing for all three time step sizes. The effects of time step are quite significant for this high-lift flow. At all pressure stations shown, URANS combined with generalized-α outperforms the other simulations in terms of pressure coefficient prediction. Massive separations over the entire main element are erroneously predicted at PS1 for RANS, and at PS5 for URANS combined with Backward Euler. Instead, URANS with generalized-α shows substantially better agreement with the experimental data at both stations, especially over the flap of the wing. Interesting, however, is the fact that at PS9 all three simulations were not able to capture the proper flow features, predicting a massive separation. This result is in agreement with other participants of the HiLiftPW-2 [5]. Moreover, at the wing-tip pressure station, notably a challenging location for RANS turbulence models, the predicted pressure is significantly improved with URANS and generalized-α. Note, in addition, that the URANS simulation with $\Delta t = 5.0 \times 10^{-5}$ s showed better agreement with wind tunnel data at the other pressure stations as well.
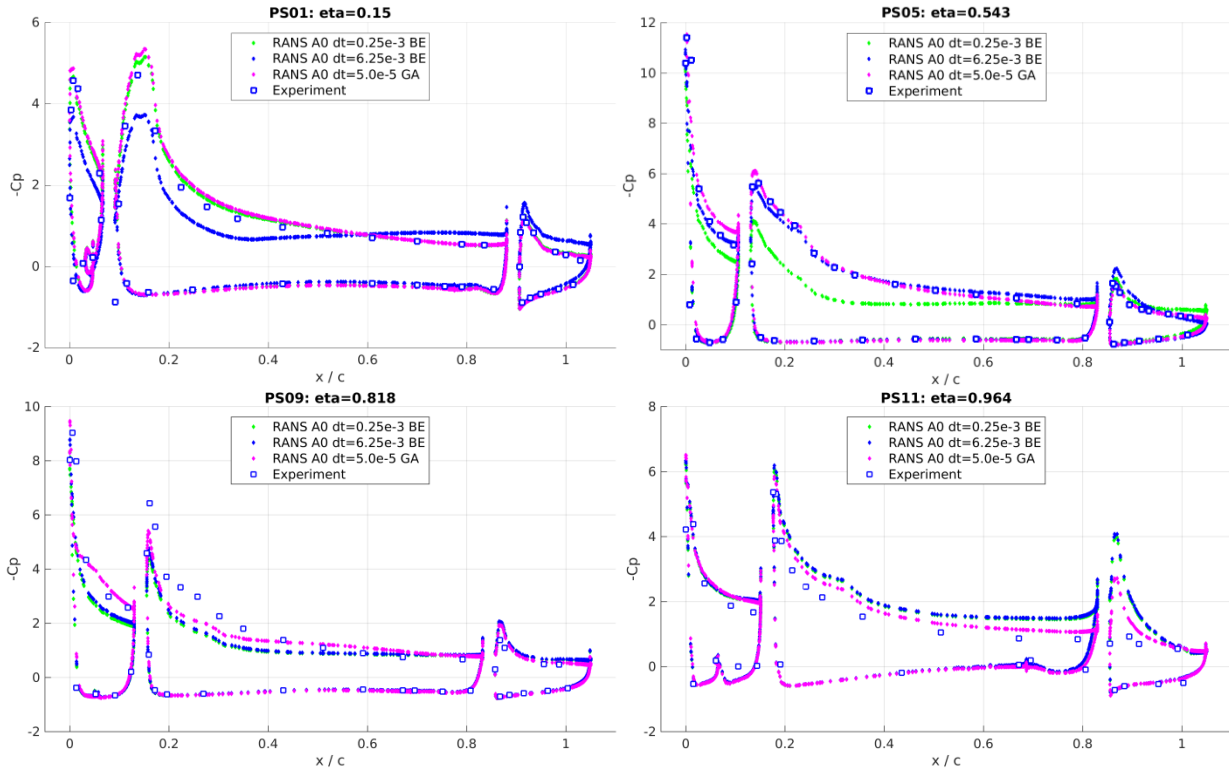
Figure 20: Pressure coefficient at different spanwise locations on the wing for RANS and URANS simulation on the A0 mesh at 21°.

The separation regions erroneously predicted by the three simulations are evident in Figure 21, while the oil flow image obtained from the wind tunnel tests at this angle of attack is presented in Figure 22. The oil flow image shows that there are two main regions of retarded flow on the main element. The largest one originates from the structures created by the fifth slat track and covers approximately 2/3 of the chord of the main element. The second is located downstream of the seventh slat track near the tip of the wing and covers approximately half of the main element. Note that the root vortex is also present along the wing-body juncture of the aircraft model. The Q-criterion isosurfaces in Figure 21 indicate that the root vortex is only properly modeled by the URANS simulations. Moreover, RANS predicts a massive region of separated flow stemming off of the second slat track which does not agree with the experiment results and is responsible for the overprediction of the pressure at PS1 seen in Figure 20. URANS with Backward Euler, while showing good agreement at the root, predicts a leading edge separation at slat track 4, thus incorrectly computing the pressure coefficient at PS5. URANS with generalized-α also predicts a separation region downstream of slat track 4, however in this case it resembles a trailing edge separation caused by the adverse pressure gradient acting on the retarded flow in the wake of the slat track. There is also a small separation pocket at the trailing edge of the main element behind slat track 5. This is the location where the wind

31

tunnel experiments show stall effects occurred on the wing, contrary to all numerical simulations. As seen from the pressure coefficient plots in Figure 19, all cases run on the A0 mesh overpredicted the experimental data at PS9. Figure 21 shows that this modeling error is due to the common prediction of leading edge separation at slat track 6. For URANS with generalized-α, this separation is slightly smaller, resulting in a slightly more accurate pressure computation on the main element of the wing at PS9.

a) RANS at $\Delta t = 6.25 \times 10^{-3}$ with Backward Euler   b) URANS at $\Delta t = 0.25 \times 10^{-3}$ with Backward Euler

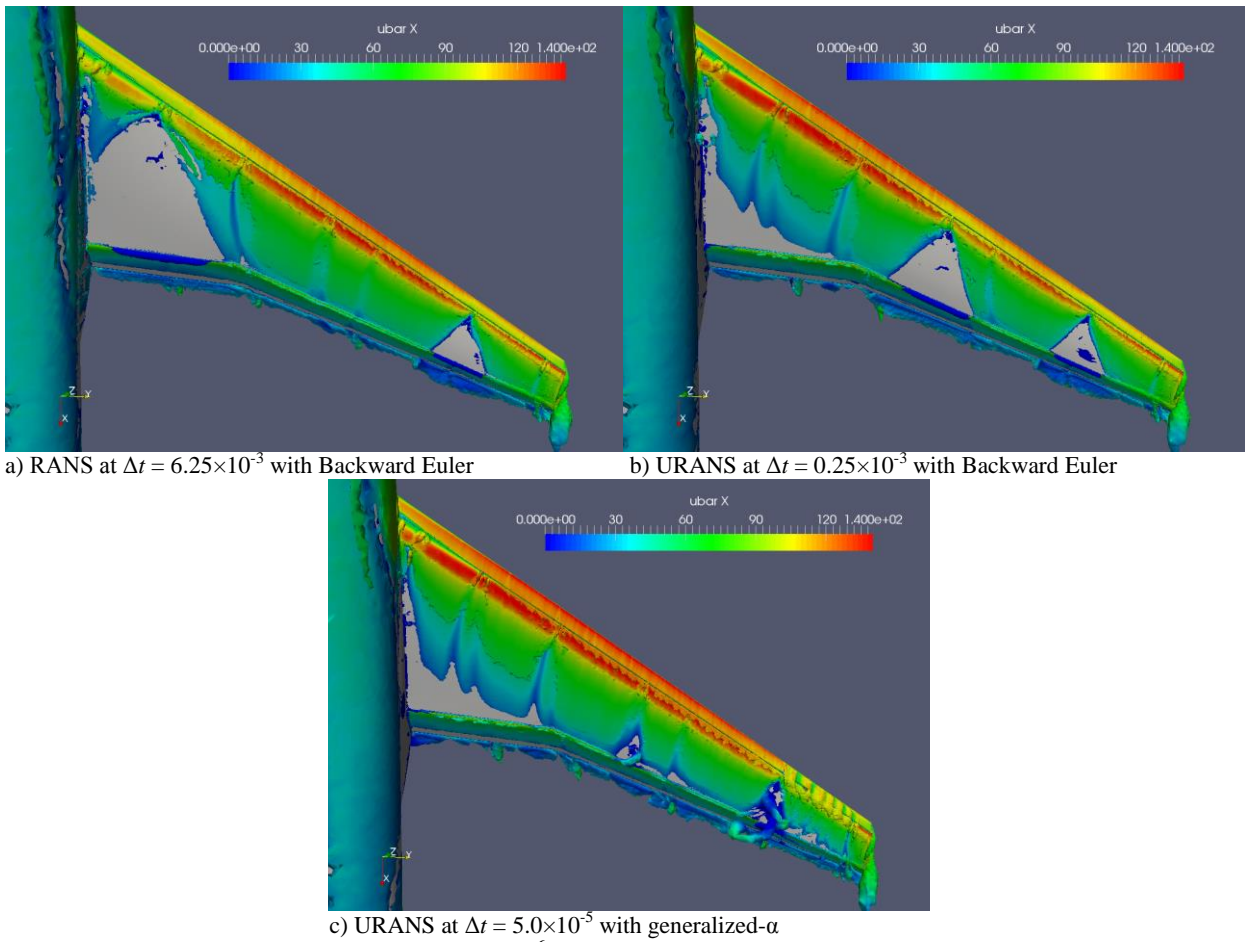c) URANS at $\Delta t = 5.0 \times 10^{-5}$ with generalized-α

Figure 21: Isosurface of the Q-criterion, Q = 1.0×10^{6}, for the RANS and URANS simulations on A0 at $21°$ angle of attack.
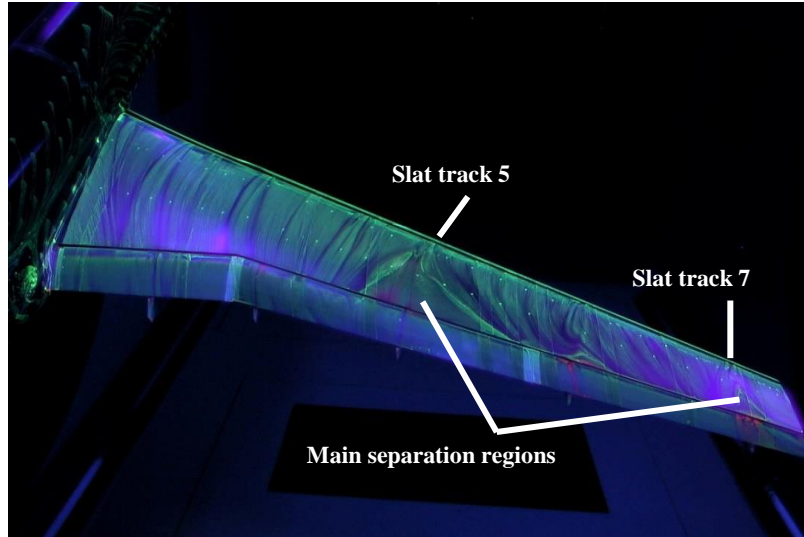
Figure 22: Oil flow image of the wing obtained during the wind tunnel experiment on the F11 geometry at 21° angle of attack.

A second time step study was performed on the A0 mesh at this angle of attack with the purpose of determining the modeling errors associated with seeking a time accurate solution only after having flushed the transient with a large RANS time step until integral quantities have reached their limit cycles. With this in mind, the final solution of the RANS simulation with $\Delta t = 6.25 \times 10^{-3}$ s and Backward Euler was used as initial condition to a fourth case with $\Delta t = 0.25 \times 10^{-3}$ s and still Backward Euler. Figure 23 shows the pressure coefficient at PS1 for both cases. Clearly, the two computations are almost identical. This result suggests that there is a form of hysteresis in the predicted flow. Improving the time accuracy in order to resolve more of the unsteady phenomena does not correct the modeling errors produced by the larger time step.

Figure 23: Pressure coefficient at PS1 for the RANS simulation and the URANS simulation with $\Delta t = 0.25 \times 10^{-3}$ s initialized from the RANS solution.

33

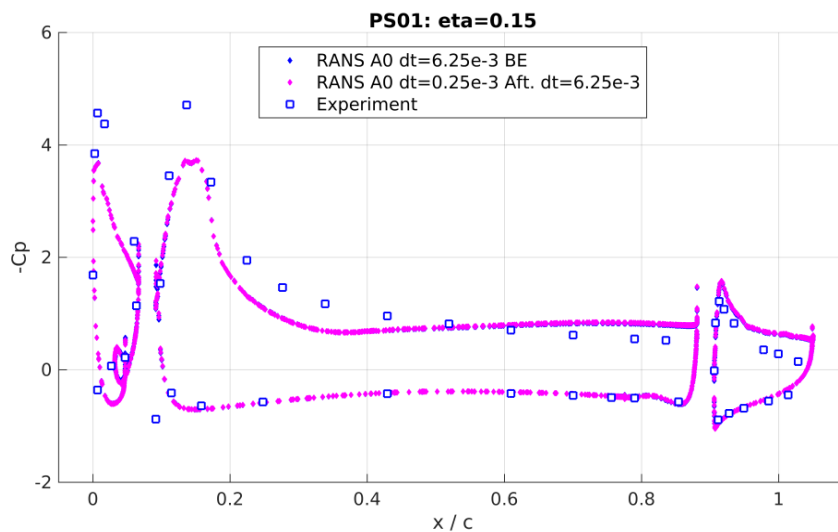The results presented here for the analysis on the A0 mesh at 21° angle of attack are a clear example of the modeling errors caused by inadequate time accuracy in the simulation. While not completely satisfying, the simulation with $\Delta t = 5.0 \times 10^{-5}$ s and the second-order accurate generalized-α method was able to model the complex physics of this high-lift flow more accurately. Instead, both RANS and URANS with the first-order accurate Backward Euler integrator showed significant modeling flaws. At these higher angles of attack where the unsteady structures of the flow play a major role in the separation dynamics (Figure 6 in Chapter 3), it is essential that when starting from zero initial conditions the transient section of the solution is not flushed out. Instead, the development of the flow must be resolved in time from the start of the simulation. Evidence for this statement is provided by results presented in Figure 19-23. In the first time step study, all three simulations started from zero initial conditions and it was shown that the simulation with the greater time accuracy matched the experimental data the best. In addition, the second time step study shows that hysteresis is present, and thus reducing the time step after a simulation with a large Δt does not change the solution. Moreover, the results of this study highlight the importance of selecting the proper time step size for flows which have significant variations in the mean flow. The time step size dictates how much averaging is performed by the RANS equations at every time step; that is whether it is just an average of the turbulence fluctuations or an average of the variations in the mean flow as well. The impact of these two levels of averaging was studied in detail by Iaccarino in reference [16], who concluded that when the flow being modeled is not statistically stationary, URANS simulations are necessary and simulations which average over the unsteadiness produce negative results. The separation regions and vortical structures generated by the slat tracks and flap fairings make this high-lift flow statistically non-stationary, thus requiring highly time accurate URANS simulations.

The reasons for the important differences observed in the prediction of the flow structures at 21° are not fully understood at this moment and require further research. It is hypothesized that the vortical structures generated by the slat tracks do not have the same time scale. These scales associated with the shedding of the vortices in the wakes differ for the many spanwise locations, and therefore a certain time step size can resolve the fluctuations for some but not for all. Future simulations will be run with time probes located in the wakes downstream of the tracks in order to identify these time scales. It is important to consider, however, the limitations of RANS turbulence models. It is known that this class of turbulence models does not perform well on flows with strong adverse pressure gradients and separation regions. Therefore it is expected that RANS and URANS simulations on this complex, 3-D,

high-lift flow reveal modeling errors. DDES simulations were also run on this configuration and showed a significant improvement in pressure coefficient prediction at all pressure stations. RANS modeling errors can therefore be eliminated with higher fidelity turbulence models, however this discussion is outside the scope of the present work.

Given what was presented here, an interesting conclusion can be drawn for this time step investigation. The numerical solution to the flow at 21° has multiple low-energy, attractive basins. Depending on the initial conditions and other parameters of the numerical method, such as time step size and integrator, the solution is attracted to one basin rather than the others. As seen from the results to the $\Delta t = 6.25 \times 10^{-3}$ s and $\Delta t = 0.25 \times 10^{-3}$ s runs, some of the basins define flows which may or may not be physical[1] but, nonetheless satisfy the equations when integrated at a particular time step from a particular initial condition. Moreover, once the solution is in one of these basins, only a large disturbance can provide sufficient energy for the solution to move to a different basin. In fact, the disturbance created by reducing the time step size was not large enough for that to happen. Later in this Chapter it will be shown that even refining the mesh does not provide a significant enough disturbance. This sensitivity to the parameters of the numerical simulation was seen only for the geometry at 21° angle of attack, not for the configuration at 7°, indicating that special modeling guidelines must be developed for high-lift flows at near-stall angles of attack. The work presented here showed that among these guidelines is the necessity of a time accurate transient phase and solution at the limit cycle which capture the unsteadiness of the vortical structures.

4.2 Grid Refinement Study

When considering the accuracy of the flow field predicted with a CFD simulation, it is important to assess whether the solution is grid independent or whether it can be improved with a refined spatial discretization. To this end, RANS simulations were run on the DLR F11 high-lift geometry at both angles of attack on the A0-URNN mesh described in Chapter 3. The 7° angle of attack geometry was also run on the A1 mesh, which was adapted from the A0 mesh using an error indicator.

---

[1] The flow fields obtained with the two larger time steps are valid solutions to the particular problem and numerical method used. These solutions can then be unrealistic and incorrect, indicating that there are flaws in the model. Alternatively, the solutions can be physically correct, and, since the simulations started from zero initial conditions, they may represent the correct flow for a different point on the hysteresis loop of the wing. There is no experimental data, however, to verify the correctness of these alternate solutions. This discussion further stresses the importance of time step when starting from zero initial conditions and attempting to predict one of the multiple solutions of high-lift flows at large angles of attack.

4.2.1   7° Angle of Attack

The time step study performed on the configuration at 7° angle of attack indicated that very similar solutions are obtained with RANS and URANS on the A0 mesh. In addition, it showed that for this relatively small angle of attack, flushing the transient and reaching a steady RANS solution does not result in major modeling errors. It was necessary to determine whether the same was true for the refined grid. Therefore, the RANS simulation on A0-URNN was kept at $\Delta t = 6.25 \times 10^{-3}$ s and Backward Euler, while the URANS simulation used $\Delta t = 5.0 \times 10^{-5}$ s and generalized-α.

The pressure coefficients computed for the simulations on A0-URNN are compared to those from the RANS case on A0 and shown in Figure 24. Only three pressure stations are shown in the figure. These are PS1, PS8 and PS11 since these were the locations where the greatest disagreement with the experimental data was seen for the results on the A0 mesh. At PS1 and PS11, thus at the root and at the wing tip, refinement had a small effect on the computed pressure and was still not able to capture the correct flow structures. This suggests that the error at these locations is not due to the mesh resolution, rather, it is due to RANS/URANS model inadequacies. At PS8, however, a significant difference can be seen. Both the RANS and the URANS simulations on A0-URNN show a noticeable improvement at the trailing edge of the wing. In particular, the pressure recovery at the trailing edge of the main element is accurately predicted, with the URANS case obtaining slightly better accuracy at the last data point. On the flap, the separation is now present and the suction peak is better represented. Again, some differences are visible between the RANS and URANS. RANS computes a lower suction peak and a larger separation region as seen by the flattening of the C_p profile closer to the leading edge of the flap. Note that at all other pressure stations the effects of refinement and increased time accuracy were negligible.

The improvements in pressure coefficient at PS8 due to refinement can be explained looking at the flow field in Paraview. The pressure profile in Figure 24 indicates that there is a region of massive flow separation on the flap, and this statement is clearly supported by the isosurface of longitudinal velocity shown in Figure 25. The large region of small longitudinal velocity, thus higher pressure, originates from the flap fairing and extends in the inboard direction crossing the plane of PS8. Comparing Figure 25 to Figure 18, the difference in size of the separation region on the flap is evident. Moreover, comparison of Figure 25 with the oil flow image in Figure 17 indicates that the predictions on the A0-URNN mesh are for more realistic. Notice also that in Figure 25 there is a region of retarded flow on the trailing edge of the main element caused by the separation region on the flap acting as an obstacle to the

www.manaraa.com

flow. This was not seen in Figure 18 for the simulations on the A0 mesh, and is what is responsible for the pressure recovery on the trailing edge of the main element. Although the retarded flow does not cross the plane of PS8 in Figure 25, isosurfaces of larger longitudinal velocity show that lower velocity fluid is present at that location. Further investigation showed that the larger separation region on the A0-URNN mesh is caused by stronger vortical structures being generated on the inboard edge of the flap fairing. These structures are visualized for simulations on both A0 and A0-URNN meshes in Figure 26. On the finer mesh, the structures start to generate further into the flap fairing cavity, and grow significantly in size as they approach the flap leading edge. Once the structures reach the gap between the flap and the main element, they are sheared and gain longitudinal velocity, becoming unstable and spreading in size over the flap upper surface. The larger and stronger vortices predicted on the finer mesh result in a larger separation, which in turn limits the acceleration of flow over the leading edge of the flap resulting in a smaller suction peak as seen in Figure 24.
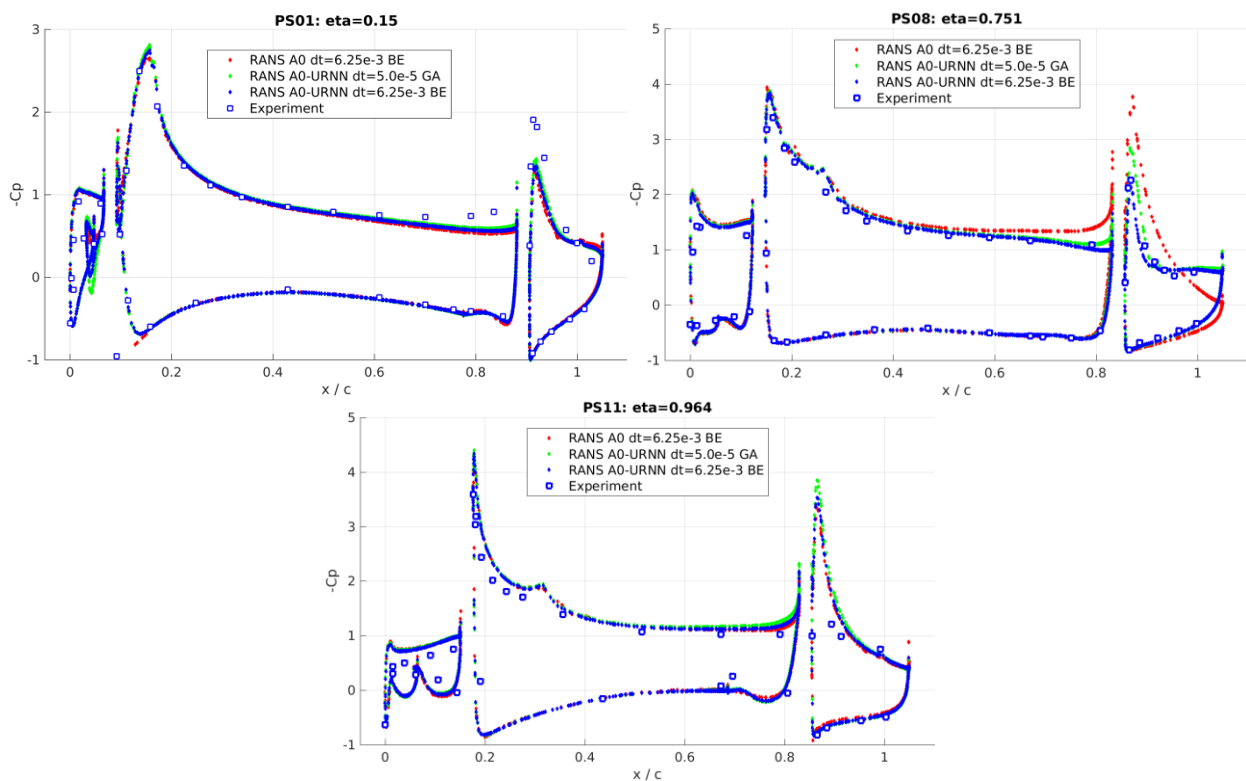

Figure 24: Pressure coefficient at different spanwise locations on the wing for RANS and URANS simulation on the A0-URNN mesh at 7°.
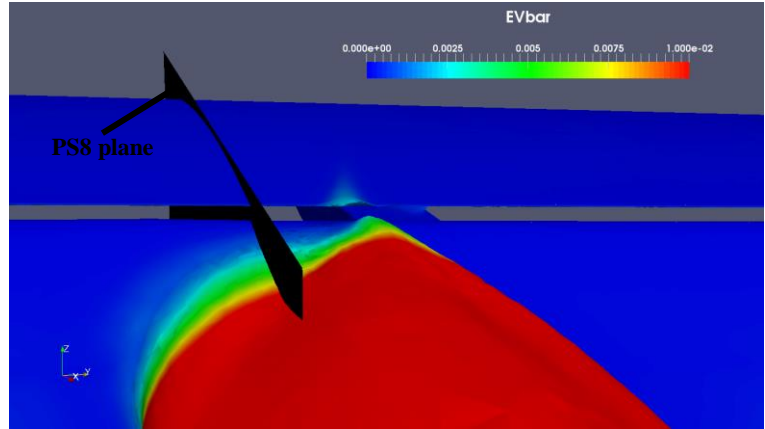
Figure 25: Isosurface of longitudinal velocity u_x = 20 m/s, around PS8 for RANS simulation on A0-URNN at 7° angle of attack.
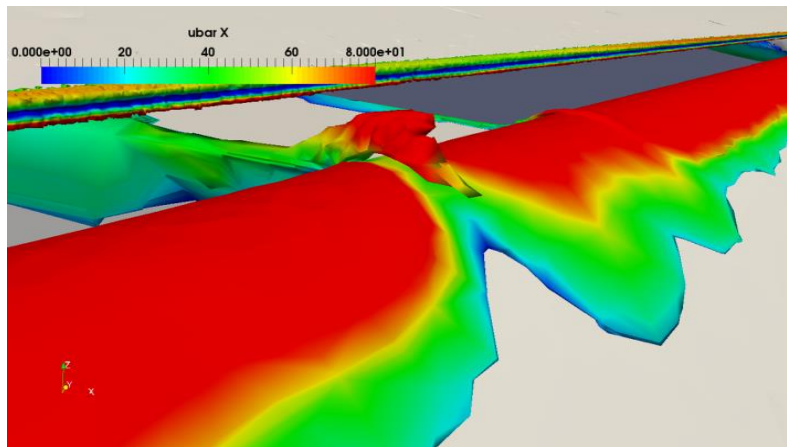
a) A0 mesh
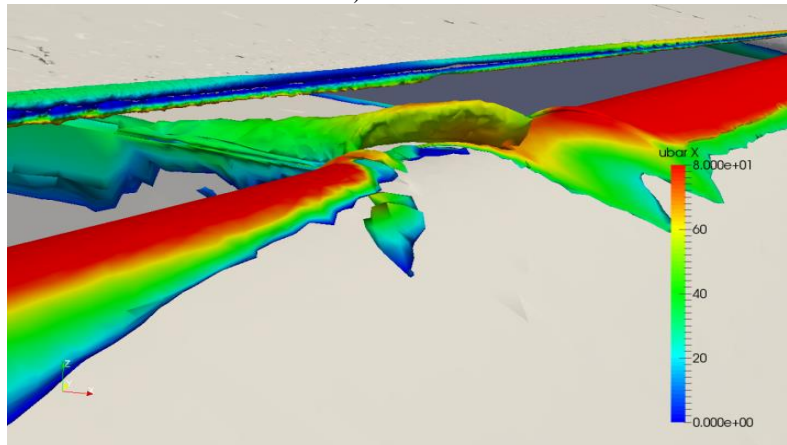
b) A0-URNN mesh

Figure 26: Isosurface of the Q-criterion, Q = 5.0×10^8, for the RANS simulations on A0 and A0-URNN at 7° angle of attack.

The results obtained on the A0-URNN mesh indicate that for the majority of the wing, the resolution of the A0 mesh was sufficient to provide a grid independent solution for RANS simulations. In other words, with the exception of the region between PS8 and PS9 around the fourth flap fairing, the spatial discretization of the A0 grid

is adequate for the RANS turbulence model used in PHASTA and increasing the resolution does not increase the predicting capability of the model. The same is not true for the region surrounding the fourth flap fairing, where the increased resolution appears to be necessary to properly model the development of the vortical structures and the flap separation. This result is of significant importance as it indicates that a uniform refinement of A0 is not necessary at this angle of attack. Rather, a local refinement is more adequate. Moreover, the very small differences in the solutions obtained with regular RANS at a large time step and URANS with second-order accurate integration suggest once again that, for the geometry at 7° angle of attack, flushing the transient and sacrificing time accuracy for computational efficiency does not result in important modeling errors. With these considerations in mind, the A1 mesh was generated as described in Chapter 3. Figure 27 shows the computed pressure coefficient for the A1 mesh at PS8 compared to the simulation on A0-URNN and the experimental data. The solutions are remarkably similar, which is to be expected because both meshes have the same resolution in the region around the fourth flap fairing. Note also that the solutions are almost identical at all other pressure stations. The A1 mesh has approximately half as many elements as the A0-URNN mesh, making error-based, local adaptation a more attractive numerical strategy for high-lift flows at small angles of attack. This number could be further reduced by restricting refinement to this region but the current error indicator also refined the wing root and tip for this case (Figure 12). These regions were larger and contributed more to the size of the mesh than the region PS8 region. This conclusion brings to light another modeling guideline for RANS simulations of high-lift flows; for angles of stack in the linear section of the lift curve, spatial resolution influences the prediction of the vortical structures responsible for the localized separation regions. These regions are not known *a priori*, therefore local, error-based adaptation is often necessary to identify the regions in need of higher resolution and improve the model predictions.

In terms of the integral quantity of interest, the simulations run on the A0-URNN and A1 meshes did not result in significant improvements in the prediction of the lift coefficient. The RANS simulation on A0-URNN with $\Delta t = 6.25 \times 10^{-3}$ s and Backward Euler overestimated the experimental value of 1.87 by 2%, while the URANS simulations with $\Delta t = 5.0 \times 10^{-5}$ s and generalized-α on both the A0-URNN and A1 meshes overestimated lift by around 3.5%.
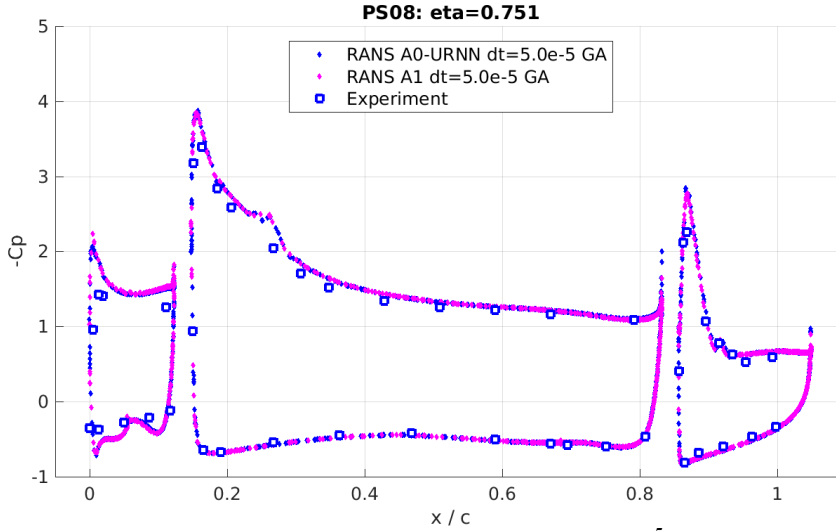
Figure 27: Pressure coefficient at PS8 for the URANS simulation with Δ*t* = 5.0×10⁻⁵ s on A0-URNN and A1 at 7° angle of attack.

4.2.2   21° Angle of Attack

The grid refinement study on the F11 geometry at 21° angle of attack involved two URANS simulations on the A0-URNN mesh. A first simulation was run with Δ*t* = 0.25×10⁻³ s and Backward Euler starting from the last time step of the simulation with the same parameters in A0 presented in the time step study. A second simulation was run with Δ*t* = 5.0×10⁻⁵ s and Backward Euler. The initial condition to this second simulation was the last time step of the first one on the A0-URNN mesh. These parameters were chosen in order to identify whether a higher resolution in both time and space was able to correct the modeling errors seen for the URANS case on A0 with Δ*t* = 0.25×10⁻³ s. Recall that the URANS simulation on A0 with Δ*t* = 0.25×10⁻³ s predicted massive leading edge separation originating at slat track four and six, and the effects of these separation region were seen more evidently at PS5 and PS9. The pressure coefficient at these two stations computed from the simulations on the refined mesh is shown in Figure 28. Clearly, refining the mesh did not improve the predicting capability of the model with reference to the experimental data. In fact, it appears that the separation regions erroneously computed by the simulation on A0 spread in size, as seen by the smaller suction peaks on the main element and by the flattening of the profile occurring closer to the leading edge. Moreover, it can be seen that the separation region changed due to the mesh refinement, and that reducing the time step size after the change was not beneficial. Note, however, that the pressure distributions at all other pressure stations, excluding PS5 and PS8, were quite similar for the two meshes. Therefore,

40

in locations where the flow was accurately predicted by the URANS simulation on A0 with $\Delta t = 0.25 \times 10^{-3}$ s, the solution is grid independent and the A0 mesh provides enough resolution for RANS to perform at its best.
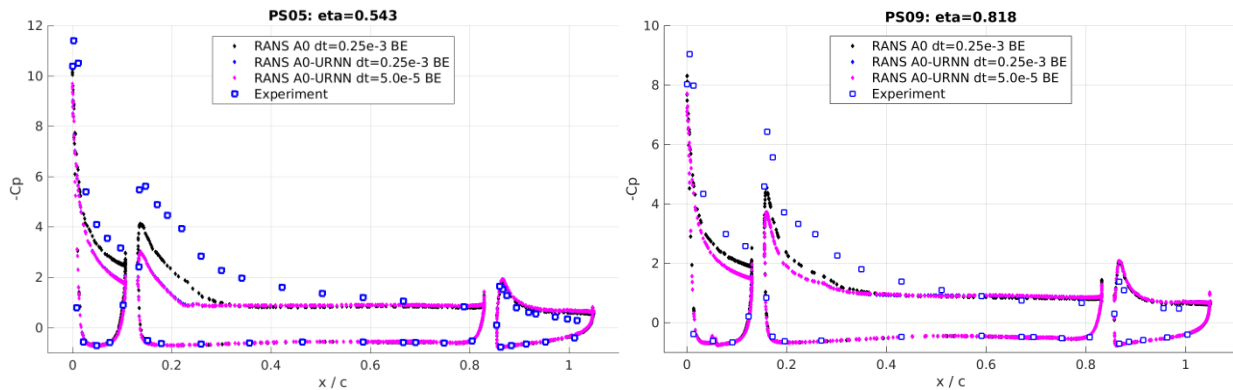

Figure 28: Pressure coefficient at PS5 and PS9 for the URANS simulations on A0-URNN at 21° angle of attack.

When analyzed in Paraview, it was seen that the difference in pressure coefficient at PS5 and PS8 between URANS with $\Delta t = 0.25 \times 10^{-3}$ s and Backward Euler on the two meshes is indeed caused by larger separation regions for the A0-URNN case. It was also observed that more vortical structures are generated by the slat track on the refined mesh compared to the initial mesh. Figure 29 shows these structures for both meshes. The vortices responsible for the leading edge separation on the main element are evident. The vortices create regions of retarded, secondary flow which reduce the velocity and the energy in the boundary layer of the main element leading edge. This is seen by the green and blue regions of the Q-criterion isosurface around the vortices. The lower energy levels in the boundary layer make it more susceptible to the adverse pressure gradient and thus more prone to becoming unstable and separating. For the simulation on A0-URNN, the structures are larger, thus the boundary layer has smaller energy and becomes unstable further upstream.
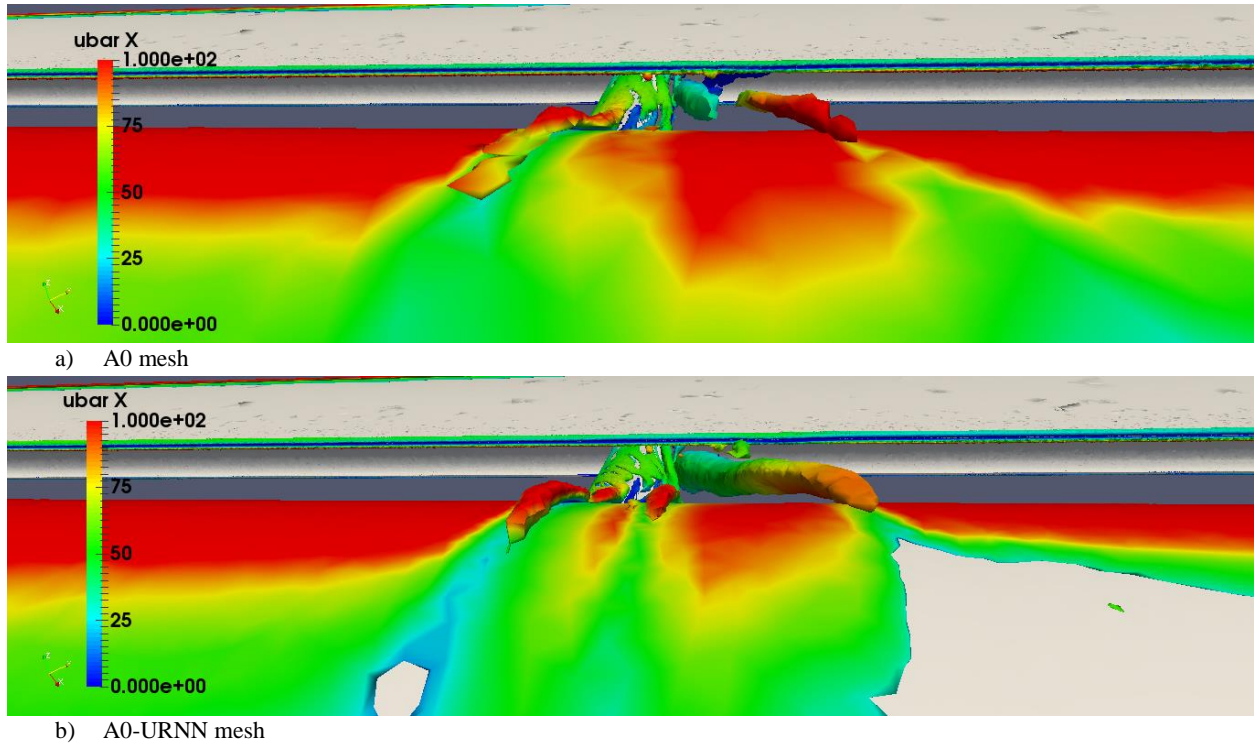
a) A0 mesh

b) A0-URNN mesh

Figure 29: Q-criterion isosurface, Q = 5.0×10⁸, at slat track four for URANS with Δ*t* = 0.25×10⁻³ s on the A0 mesh (top) and the A0-URNN mesh (bottom).

The following conclusion can be drawn from the results for the grid refinement study on the F11 geometry at 21° angle of attack: if the solution on the initial mesh presents significant modeling errors, an increase in resolution is likely can have a negative effect on the predictive capability of the model. This statement carries significant importance, and further highlights the modeling guidelines established from the time step study. When modeling turbulent flows with RANS simulations, grid refinement is employed to verify mesh independence of the solution, as well as to improve the accuracy of the numerical computation. However, it was shown in Figure 28 and Figure 29 that for this high-lift flow, refinement does not have a beneficial effect when significant modeling errors from other sources (e.g., hysteresis from time step and/or model deficiency) are present. Consequently, the necessity to perform a time accurate simulation on the initial mesh resolving the unsteady features is heightened. Modeling errors generated by inadequate time stepping in the startup cannot be removed by a reduction in time step or an increase in resolution. The hysteresis that is present for the erroneous solutions to the flow cannot be overcome with grid refinement. Relating back to the concept of the low-energy attractive basins mentioned in the discussion of the time step study for this angle of attack, mesh refinement does not provide a large enough disturbance for the solution to

42

leave the region of influence of the basin it has converged to. Note that these conclusions are valid for the F11 geometry at 21° angle of attack, which is representative of a post-stall condition.

It was shown earlier that for the model at 7° angle of attack, grid refinement can indeed be beneficial. Interestingly, however, Figure 24 showed that grid refinement on the 7° case did not improve prediction of the pressure coefficient at PS1. Recall for this angle of attack the computations overpredicted the size of the root vortex which lead to the increased pressure on the trailing edge of the wing. This, combined with the results form Figure 28, suggests that, regardless of the angle of attack, mesh refinement does not improve the flow prediction if the vortical structures are already overpredicted on the initial mesh. Other modeling strategies are thus necessary, one if which is the implementation of the higher fidelity DDES turbulence model.

Finally, as expected from the pressure coefficient plots in Figure 28, the lift force computed for both URANS simulations on the A0-URNN mesh at 21° angle of attack was within 1% of the value computed for the simulation on A0 with $\Delta t = 0.25 \times 10^{-3}$ s at the same incidence. The predicted lift, however, was larger for the A0-URNN computations than those on A0, despite of the larger separation regions on the suction surface of the main element.

Chapter 5

Conclusions and Future Work

The work presented in this report employed a time step study and a mesh refinement study to outline some of the modeling guidelines for RANS CFD simulations of high-lift flows at different angles of attack, namely 7° and 21°. The DLR F11 geometry was selected as a test case for commercial aircraft in lading configuration, with slats and flaps deployed on the wing. The model utilized in the simulations included the supports to connect the slat and flap to the main element of the wing. The results obtained indicated that for the geometry at 7° angle of attack, time step does not have a significant effect on the predicting capability of the model and therefore it is possible to select a large time step (on the order of 5×10^{-3} s) to flush out the transients and reach a steady RANS solution. In addition, it was shown that mesh refinement can be a valuable tool to improve the flow prediction in areas where the solution on the initial mesh presented modeling errors. Furthermore, since the initial mesh provided enough resolution on the majority of the wing, error-based, local adaptation was found to be more efficient than uniform refinement of the entire grid and just as accurate.

For the F11 geometry at 21° angle of attack, the observations made were quite different. The time step study showed that time accuracy for both the transient phase and in the limit cycle is important in order to avoid significant modeling errors in the solution. In this post-stall configuration, the unsteady structures generated from the slat and flap supports have a significant impact on the separation dynamics of the wing. Therefore, a time step size adequate to capture these unsteady fluctuations is required for accurate modeling. Moreover, it was identified that the flow features erroneously predicted by an inadequate time step size suffered from hysteresis, meaning that neither an increase in time accuracy, nor an increase in mesh resolution were able to provide a correction.

The first step for the continuation of the work done in this project is to improve the fidelity of the geometric model used in the simulations. The model used in this work contained the flap and slat supports, however it did not contain the pressure tube bundles on the slat tracks contrary to the experimental geometry. It was shown experimentally that the additional obstacles provided by the tubes have a non-negligible effect on the lift curve of the F11 wing at large angles of attack. Therefore, simulations on the higher fidelity geometry should be run to identify the impact of the increased obstruction on the flow. It is expected that the modeling of the tubes will provide

a better match between the numerical results and the experimental data because the unsteady vortical structures will be represented more accurately.

Following the improvement of the geometric model, a study of the time scales of the vortical structures generated by the slat tracks and tube bundles should be performed. This would allow to identify how the time step selected for the CFD simulation compares to the fluctuations in the mean flow due these supports, and therefore how much averaging is performed by the RANS turbulence model. As shown by Durbin and by the work presented here, if the time step is too large and omits the effects of the fluctuations, significant modeling errors can occur. Consequently, understanding the time scales of the unsteady features would lead to the selection of a time step size capable of capturing the required unsteady features and improve the prediction of this high-lift flow at large angles of attack.

Bibliography

[1] T. Holl at al., "Detached-Eddy Simulation of Pulsed Blowing Actuation on the Flap of a High-Lift Configuration," *29th AIAA Applied Aerodynamics Conference*, Honolulu, 2011.

[2] J. P. Slotnick, J. A. Hannon, M. Chaffin, "Overview of the First AIAA CFD High Lift Prediction Workshop (Invited)," *49th AIAA Aerospace Sciences Meeting*, Orlando, 2011.

[3] R. Rudnik, K. Huber, S. Melber-Wilkending, "EUROLIFT Test Case Description for the 2nd High Lift Prediction Workshop," *30th AIAA Applied Aerodynamics Conference*, New Orleans, 2012.

[4] C. L. Rumsey et al., "Summary of the First AIAA CFD High Lift Prediction Workshop (invited)," *49th AIAA Aerospace Sciences Meeting, Orlando*, 2011.

[5] C. L. Rumsey, J. P. Slotnick, "Overview and Summary of the Second AIAA High Lift Prediction Workshop (Invited)," *Journal of Aircraft*, Vol. 52, 2015, pp. 1006-1025.

[6] S. Deck, "Zonal-Detached-Eddy Simulation of the Flow Around a High-Lift Configuration," *AIAA Journal*, Vol. 43, No. 11, November 2005.

[7] M. Rasquin, "Parallel Adaptive Detached Eddy Simulations of the EUROLIFT DLR-F11 high lift configuration," *32nd AIAA Applied Aerodynamics Conference*, Atlanta, 2014.

[8] T. J. R. Hughes, *The Finite Element Method: Linear Static and Dynamic Finite Element Analysis*, Dover Publications, New York, 2000, p. 7.

[9] C. H. Whiting, K. E. Jansen, "A stabilized finite element method for the incompressible Navier-Stokes equations using a hierarchical basis," *International Journal for Numerical Methods in Fluids*, No. 35, 2001, pp. 93-116.

[10] C. H. Whiting, "Stabilized Finite Element Methods for Fluid Dynamics using a Hierarchical Basis," PhD Thesis, Rensselaer Polytechnic Institute, 1999.

[11]] K. E. Jansen, C. H. Whiting, G. M. Hulbert, "A generalized-α method for integrating the filtered Navier-Stokes equations with a stabilized finite element method," *Computer methods in applied mechanics and engineering*, No. 190, 2000, pp. 305-319.

[12] K. E. Jansen, Private communications, 2016.

[13] P. R. Spalart, S. R. Allmaras, "A One-Equation Turbulence Model for Aerodynamic Flows," *30th Aerospace Sciences Meeting and Exhibition*, Reno, 1992.

[14] Simmetrix Inc., www.simmetrix.com.

[15] P. R. Spalart, "Young-person's guide to detached-eddy simulation grids," *National Aeronautics and Space Administration*, 2001.

[16] G. Iaccarino, A. Ooi, P. A. Durbin, M. Behnia, "Reynolds averaged simulation of unsteady separated flow," International Journal of Heat and Fluid Flow, Vol. 24, Issue 2, Apr. 2003, pp. 147-156.

[17] Paraview, www.paraview.org.